Mineralium Deposita
https://doi.org/10.1007/s00126-023-01209-4

ARTICLE

Genesis of copper mineralization in the polymetallic tin deposits from the Herberton Mineral Field, Queensland, Australia

Avish Kumar[1] · Ioan Sanislav[1] · Laure Martin[2] · Matvei Aleshin[2] · Paul Dirks[1]

Received: 31 January 2023 / Accepted: 23 August 2023

Abstract

The Herberton Mineral Field hosts multiple small-scale, polymetallic Sn-Cu and Sn-Zn deposits. The Baal Gammon and Isabel polymetallic deposits in the Herberton Mineral Field contain early Sn that is overprinted by sulfides. At Baal Gammon, the sulfide overprinting is Cu-In-rich, whereas Isabel is a Zn-Pb-In-rich system. These deposits are hosted in the meta-sedimentary rocks of the Hodgkinson Formation and the porphyry dikes and volcanic rocks of the Kennedy Igneous Association. Primary Sn in these deposits occurs as cassiterite, which was altered to stannite during sulfide mineralization. The sulfide ores from Baal Gammon consist of chalcopyrite, pyrrhotite, and minor sphalerite, and sphalerite, galena, and minor chalcopyrite are observed at Isabel. Chalcopyrite from Baal Gammon contains on average 609 ppm Ag, 1194 ppm In, and 1410 ppm Sn, whereas chalcopyrite from the Isabel deposit contains on average 2302 ppm Ag, 725 ppm In, and 1042 ppm Sn. Sulfur isotope ($\delta^{34}S$) measurements of in-situ chalcopyrite-pyrrhotite mineral pairs show limited variation and low values that are indicative of a magmatic sulfur source with limited interaction with sulfur from connate and meteoric fluids during mineralization. The chalcopyrite and pyrrhotite $\delta^{34}S$ values at the Baal Gammon deposit vary between 0.99–1.91‰ and 1.35–2.48‰, respectively. The $\delta^{34}S$ values at the Isabel deposit vary between 0.91–1.45‰ for chalcopyrite and 1.12–2.11‰ for pyrrhotite. The trace element composition of major sulfides and sulfur isotopes of chalcopyrite and pyrrhotite combined with thermodynamic modeling indicates that the mineralizing fluids at the Baal Gammon and Isabel deposits have an igneous source, where the metals were transported as metal-chloride complexes at low pH (< 5) and below ~ 300 °C. The source of these sulfide-rich mineralizing fluids is most likely derived from the magmatic activity associated with the emplacement of the Slaughter Yard Creek Volcanics during a period of crustal thinning between 300 and 280 Ma.

Keywords Sulfur isotope · Copper · Critical metals · Physicochemical modeling · Queensland

Introduction

Copper is an essential metal for our existing and changing economy. It is used in electric vehicle batteries, motors, wiring, and battery charging hubs (Nguyen et al. 2021). Copper is mined from several deposit types, including volcanogenic massive sulfide (VMS; Mosier et al. 2009; Tornos et al. 2015), Cu±Mo±Au porphyry (Kirkham and Sinclair 1995; Sillitoe 2010), skarn (Meinert 1992; Xie et al. 2020), iron oxide copper-gold (IOCG; Skirrow 2022), magmatic Cu-Ni (Barnes and Lightfoot 2005; Eckstrand and Hulbert 2007), sediment-hosted copper (Brown 1997, 2014; Rajabpour et al. 2017a), and polymetallic veins (Han et al. 2006; Kojima et al. 2009). The best studied and most extensively explored deposit types are the copper porphyry (69% of global Cu production), sediment-hosted copper (12% of global Cu production), and IOCG (4.7% of global Cu production) deposits, and they constitute the largest sources of copper (Richards 2016; Singer 2017; Chiaradia and Caricchi 2022). The increasing demand for copper has raised concerns regarding its future availability (Elshkaki et al. 2016) and has created opportunities for exploration and mining of smaller scale deposits that occur as polymetallic veins. The research and exploration of polymetallic Sn-Cu deposits are important

Editorial handling: S. Hagemann

✉ Avish Kumar
avish.kumar@my.jcu.edu.au

[1] Economic Geology Research Centre (EGRU), College of Science and Engineering, James Cook University, Townsville, Queensland, Australia

[2] Centre for Microscopy, Characterisation and Analysis, University of Western Australia, Perth, Australia

Published online: 20 September 2023

since they also host critical metals, which are necessary for the functionality of emerging technologies but have supply constraints (Watari et al. 2020), such as In, Sn, W, Bi, and Li (Dill et al. 2013; Torres et al. 2019; Zhou and Wen 2021).

The Herberton Mineral Field (HMF) in Northeast Queensland, Australia, contains a variety of polymetallic Cu deposits, which occur as veins associated with Sn-W mineralization (Fig. 1). Similar deposit styles have been recognized in the Bolivian Sn belt, the Gejiu Sn district in China, and the Camborne-Redruth-St. Day Sn district in England (Sillitoe and Lehmann 2022). A common feature of these metallogenic provinces is that the mineralization is associated with fractionated granites, and displays a well-developed metal zonation, in which Sn, W, Mo, and Cu enrichment is proximal, and Zn, Pb, and Ag occur more distal to the intrusion (Taylor and Cuff 1979; Audétat et al. 2000). In these systems, the different metals may have different sources, with Sn mineralization genetically associated with reduced granitoids (Ishihara 1981; Eugster 1985; Harlaux et al. 2021a; Wu et al. 2021) and Cu with oxidized magmas (Murakami and Ishihara 2013). Tin is generally deposited at higher temperatures (~ 500 °C; Kelly and Turneaure 1970; Lehmann 2021) than Cu (~ 300–400 °C; Sun et al. 2013; Richards and Mumin 2013; Gómez et al. 2021).

Metals in magmatic-hydrothermal systems are generally transported under acidic to near neutral conditions as complex ions of chlorine and hydrosulfide (Liu and McPhail 2005; Etschmann et al. 2010; Richards 2011). Typically, metal deposition occurs as a result of changes in temperature, pH, oxidation state, and sulfur fugacity, which can lead to the destabilization of metal complexes and promote metal precipitation (Pokrovski et al. 2013; Schaarschmidt et al.

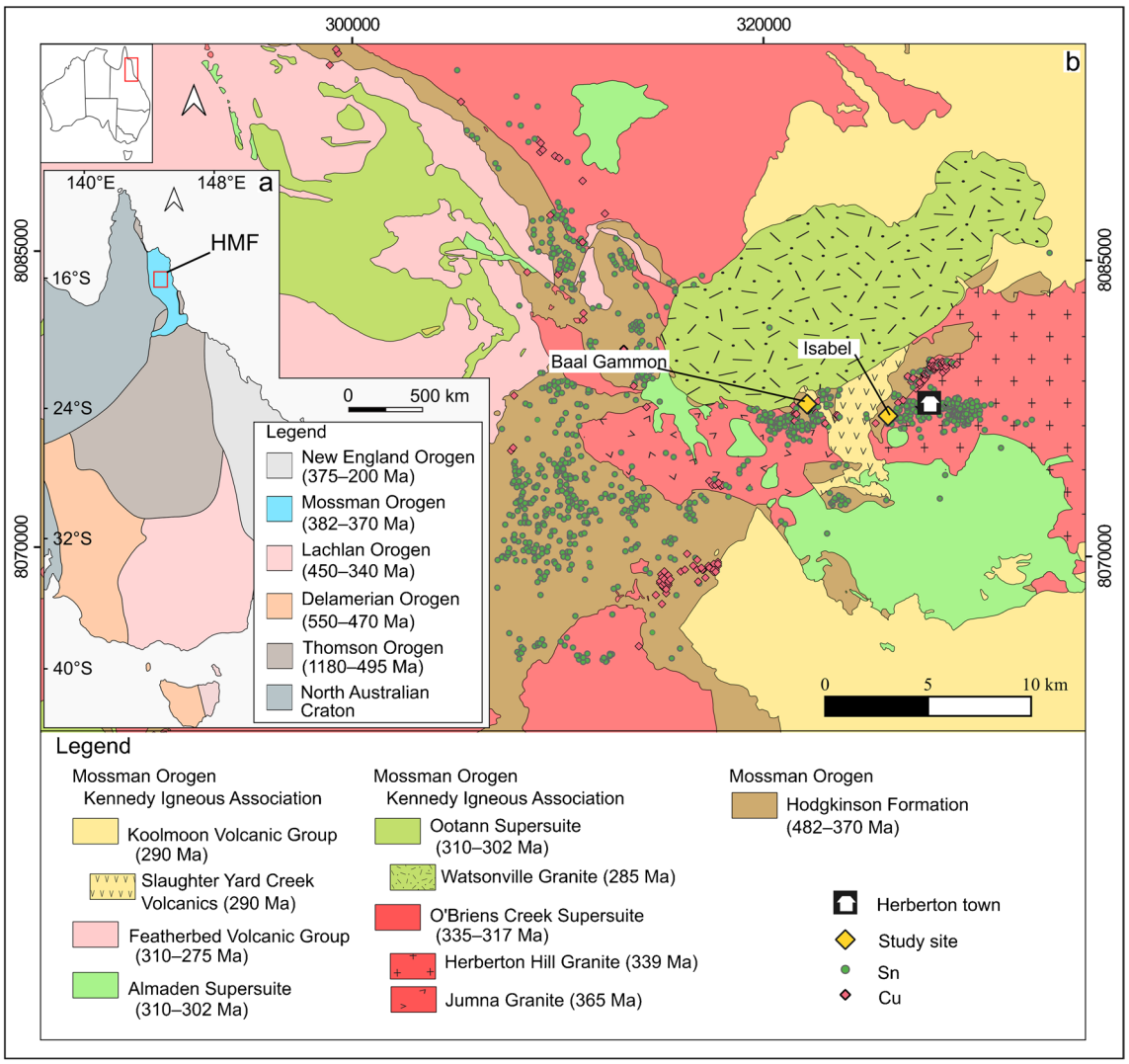

Fig. 1 **a** Outline of orogens in eastern Australia and the HMF. **b** Simplified geological map of the HMF. The age data shown in the legends are from U-Pb zircon geochronology compiled from Purdy et al. (2016), Cheng et al. (2018), and Kumar et al. (2022)

2021). The evolving hydrothermal conditions during ore deposition are complex, but important geochemical information can be recovered through detailed studies of mineral parageneses, mineral chemistry, and stable isotopes (e.g., sulfur and oxygen) of ore and alteration minerals (Rajabpour et al. 2017b; Li et al. 2020; Fitzherbert et al. 2021; Tashi et al. 2021).

Sulfur isotopes, especially for mineral pairs, provide a powerful geochemical tool to track the sulfur source and constrain fluid interaction and temperature of sulfide deposition (Ohmoto 1972; Seal 2006; Farquhar et al. 2010; Shanks et al. 2014; Walker et al. 2019). The $\delta^{34}S_{V\text{-}CDT}$ values associated with magmatic processes in mid-ocean ridge basalts from the Pacific-Antarctic ridge range from − 1.57 to + 0.06‰, and the deviation from the 0.0‰ mantle-like signature is due to mixing of depleted mantle and recycled oceanic crust (Labidi et al. 2014). In contrast, $\delta^{34}S$ associated with sedimentary processes have a wide variation in isotopic signature and vary from − 50 to + 20‰ (Tostevin et al. 2014). These variations in sulfur isotope values are reflected in the sulfide minerals associated with ore deposits.

In this study, we investigate the hydrothermal processes that were involved in the formation of the polymetallic Baal Gammon and Isabel deposits using thermodynamic modeling in combination with studies on mineral paragenesis, mineral chemistry, and sulfur isotopes. These deposits are ideal for studying hydrothermal processes that operated during the formation of polymetallic vein deposits that consists of Sn-Cu and Sn-Zn styles of mineralization.

Geological setting

Regional geology

The Tasmanides are a series of orogenic belts that extend from South Tasmania to far North Queensland, as part of the Terra Australis Orogen (Fig. 1a; Cawood 2005). They encapsulate the geological history of eastern Australia from the Cambrian to the Triassic and record evidence for the breakup of Rodinia, the formation of Gondwana, the collision of Gondwana and Laurasia to form Pangea, and the breakup of Pangea (Glen 2005; Klootwijk 2013). The orogenic belts within the Tasmanides include the Delamerian, Thomson, Lachlan, Mossman, and New England Orogens (Fig. 1a; Rosenbaum 2018). The Delamerian Orogen is best exposed in the southern part of the Tasmanides, and it formed from the middle Cambrian to the early Ordovician (550–470 Ma), mostly as a result of contractional deformation (Flöttmann et al. 1994, 1998; Foden et al. 2020). The Lachlan Orogen (450–340 Ma) is positioned east of the Delamerian Orogen and consists of thrust fault systems developed in a turbidite-dominated sequence (VandenBerg 1999; Gray and Foster 2004; Hough et al. 2007). The Thomson Orogen (1180–495 Ma) is poorly exposed, as it lies under a cover of younger sedimentary basins, except for a series of metamorphic terranes in North Queensland that consist of Neoproterozoic to Early Paleozoic volcano-sedimentary sequences (Glen et al. 2013; Spampinato et al. 2015b; Spampinato et al. 2015a; Purdy et al. 2016; Cross et al. 2018; Dirks et al. 2021; Edgar et al. 2022a, 2022b; 2023). The Mossman Orogen temporally overlaps with the New England Orogen and encompasses convergent margin rocks that are mostly composed of marine sediments (Henderson et al. 2013) intruded by Carboniferous and Permian granitoids with associated volcanics (Champion 1991; Cheng et al. 2018; Kumar et al. 2022). The New England Orogen (375–200 Ma) is the youngest orogen and consists of multiple cycles of compression and extension (Jessop et al. 2019). The Tasmanides are extensively mineralized with precious (Au), base (Cu, Pb, and Zn) and critical metals (Kumar et al. 2022).

Geology of the Herberton Mineral Field

The HMF is situated in the Mossman Orogen and contains Au, Cu, Zn, Sn, W, Mo, and critical metal deposits (ca. 2400 lode deposits; Blake 1972). These deposits are hosted by metasedimentary rocks of the Hodgkinson Formation and felsic rocks of the Kennedy Igneous Association (Fig. 1b; Cheng et al. 2018; Kumar et al. 2022). The Mossman Orogen consists of a multiply deformed turbidite sequence (the Hodgkinson Formation) in the east, and fossiliferous limestone, chert, meta-basalt, and sandstone of the Chillagoe Formation in the west (Withnall and Henderson 2012; Henderson et al. 2013). The Kennedy Igneous Association comprises granitoids and volcanic rocks that have been grouped into four supersuites, based on petrological similarities (White et al. 2001), which intruded the Hodgkinson Formation. Rocks belonging to three of these supersuites occur near the Baal Gammon and Isabel deposits (Fig. 1b). The O'Briens Creek Supersuite, which is the oldest, hosts most of the Sn and W deposits and consists of highly fractionated granites with U-Pb zircon ages between ca. 365 and 317 Ma (Champion 1991; Cheng et al. 2018; Kumar et al. 2022). The Ootann Supersuite is widespread in the HMF and records U-Pb zircon ages of between 320 and 302 Ma (Champion and Chappell 1992; Cheng et al. 2018). The Almaden Supersuite mostly consists of granodiorite and is the youngest with U-Pb zircon ages at ca. 300 Ma (Champion and Chappell 1992). Two volcanic units, the Featherbed Volcanics and the Koolmoon Volcanic Group, occur near the Baal Gammon and Isabel deposits (Fig. 1b). The Featherbed Volcanics (310–275 Ma; Cheng et al. 2018) extend to the western part of the HMF and lie over the Ootann Supersuite, whereas the Koolmoon Volcanic Group (ca. 290 Ma; Kumar et al. 2022) occurs mainly in the eastern section overlying the Almaden and O'Briens Creek Supersuites (Fig. 1b).

Geology of the Baal Gammon deposit

The Baal Gammon deposit consists mainly of Cu(+Zn-In) mineralization that overprints earlier Sn and is hosted in the meta-sedimentary rocks of the Hodgkinson Formation and in the United North Australian Mine Porphyry (UNA Porphyry; Fig. 2a, b). The UNA Porphyry intruded the meta-sedimentary rocks as an irregularly shaped dike. The meta-sedimentary rocks consist of fine- to coarse-grained sandstone that dip gently to the SW with bedding-parallel fractures and shear zones that dip 20–40° to the SW. Both the meta-sedimentary rocks and the UNA Porphyry are crosscut by quartz-feldspar porphyry dikes mapped as part of the Slaughter Yard Creek Volcanics (Kumar et al. 2022; Fig. 2a, b). Regionally, the Slaughter Yard Creek Volcanics trend NNW-SSE, but locally in the Baal Gammon open pit, they trend approximately E-W. They are also affected by hydrothermal biotite and chlorite alteration.

Three stages of mineralization are recognized in the Baal Gammon deposit. Stage I consists of Sn mineralization hosted within the greisenized UNA Porphyry as hydrothermal cassiterite (Fig. 2c). Stage II consists of Cu, Zn, and In mineralization in the form of massive to semi-massive sulfides, sulfide infill breccia, sulfide veins (Fig. 2d), and disseminated sulfides that are located in the UNA porphyry and along the contact of the UNA Porphyry and the meta-sedimentary rocks. Stage III mineralization consists of supergene alteration of the sulfide mineralization and occurs as Cu-Fe oxides and carbonates (Fig. 2e).

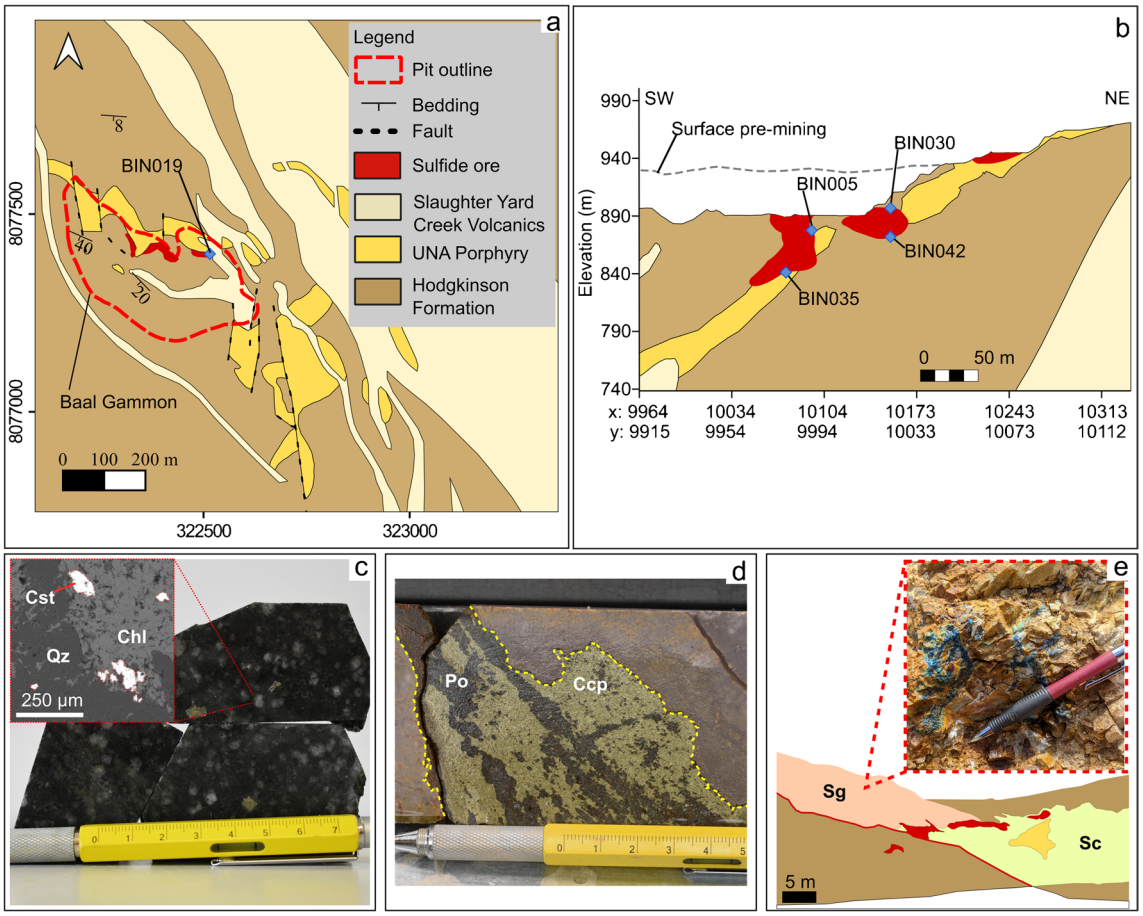

Fig. 2 **a** Simplified geological map of the Baal Gammon deposit. **b** Simplified cross-section showing mineralization overprinting the UNA Porphyry. **c** Hand-sample of the UNA Porphyry with an electron-backscatter image insert showing cassiterite (Cst) surrounded by chlorite (Chl) and quartz (Qz). **d** Drill core sample of chalcopyrite (Ccp) and pyrrhotite (Po) vein cross-cutting UNA Porphyry. **e** Simplified geological sketch map of the northern pit wall showing silica-cap (Sc) surrounding the UNA Porphyry and the supergene (Sg) zone with an insert image of copper carbonates

Geology of the Isabel deposit

The Isabel deposit contains early Sn that is overprinted by Zn-Pb-Ag-In mineralization in the form of polymetallic veins hosted by brecciated meta-sedimentary rocks of the Hodgkinson Formation (Fig. 3a, b). Fault-controlled breccia surrounds the deposit and consists of angular meta-sandstone clasts with a jigsaw-fit texture within a fine-grained quartz-feldspar matrix. Dolerite and felsic porphyry dikes, mapped as part of the Slaughter Yard Creek Volcanics, intruded the meta-sedimentary rocks. The hydrothermal breccia surrounding the polymetallic veins consists of angular meta-sandstone clasts with a jigsaw-fit pattern, with fine-grained sulfide mineralization as infill (Fig. 5d).

The polymetallic vein contains an early stage of Sn in the form of cassiterite (stage I), overprinted by a later stage (stage II) of Zn-Pb-In mineralization as sulfides (Figs. 3c and 4b). The stage I cassiterite was observed mostly as inclusions in sphalerite veins. Stage II sulfide mineralization consists of SW-NE oriented, large (10 m long and 1–2 m wide), sphalerite-rich veins, which were crosscut by thin chalcopyrite-pyrrhotite veins (Fig. 5e), sphalerite and galena veins with stannite (Fig. 5f), and hydrothermal breccia with sphalerite infill.

Materials and methods

Samples

The Baal Gammon samples (Fig. 2a, b) were taken from sulfide veins in the deeper sections of the UNA Porphyry (BIN035), from massive sulfides located at the contact between a quartz-feldspar porphyry dike and the UNA Porphyry (BIN019), and from massive sulfide mineralization that occurs at the contact between meta-sedimentary rocks and the UNA Porphyry (BIN005, BIN030, and BIN042). The Isabel samples (Fig. 3b) were taken from sphalerite veins (IN013 and IN049) and from a hydrothermal breccia (IN024) with sphalerite infill. Trace elements were analyzed for sulfides from all samples, whereas sulfur isotopes were analyzed for chalcopyrite-pyrrhotite pairs from samples BIN035, BIN005, BIN019, and IN013.

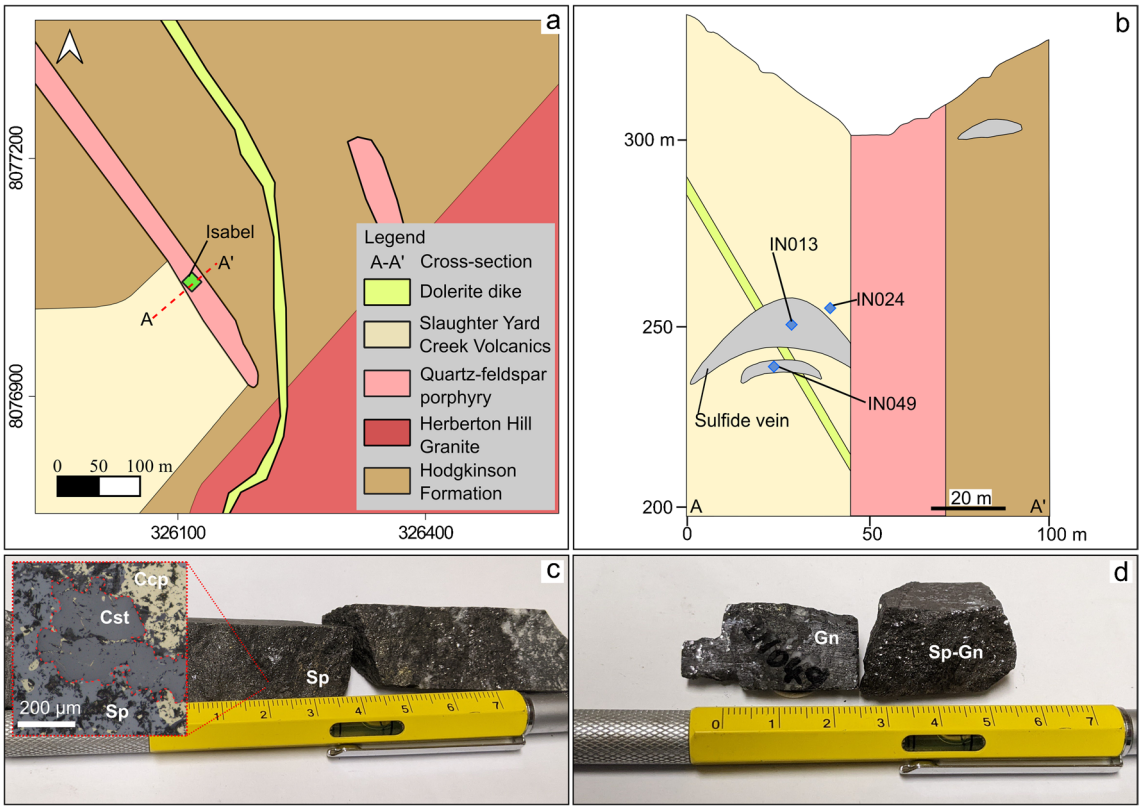

Fig. 3 **a** Simplified geological map and **b** cross-section of the Isabel deposit. **c**, **d** Drill core sample of sphalerite (Sp) and galena (Gn) veins with an insert of a photomicrograph in reflected light of cassiterite (Cst) surrounded by sphalerite (Sp) and chalcopyrite (Ccp)

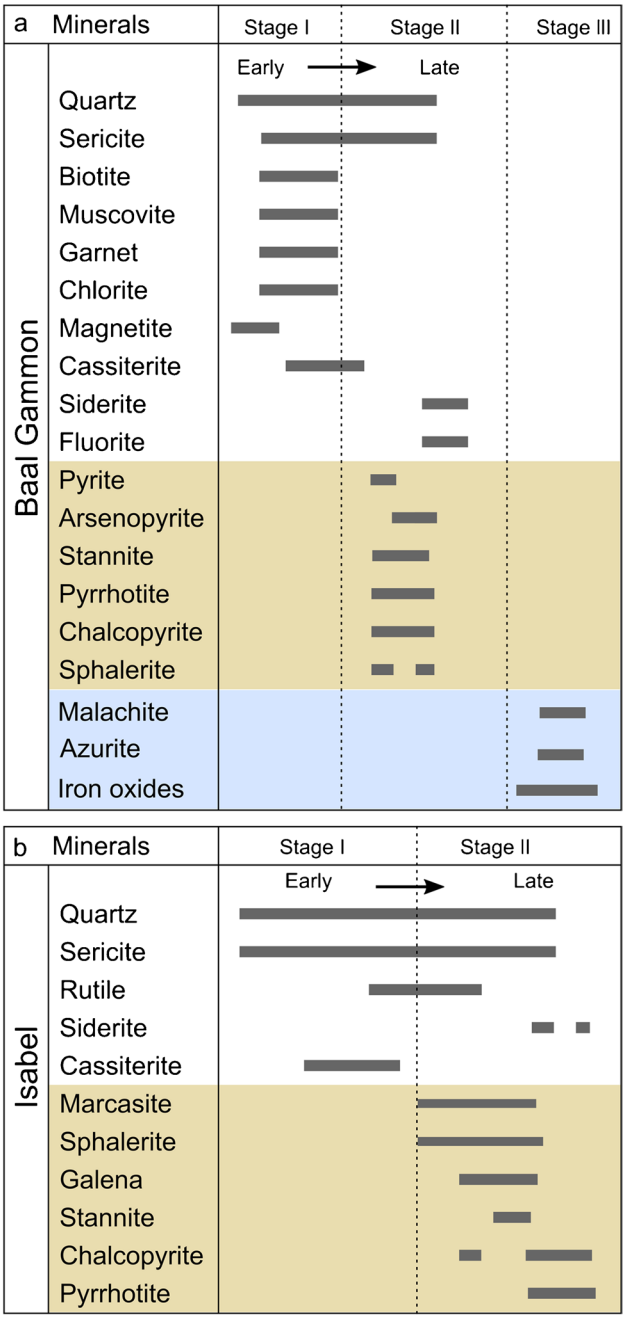

Fig. 4 Mineral paragenetic sequences for the: **a** Baal Gammon deposit and **b** Isabel deposit

Laser-ablation inductively coupled plasma mass spectrometry (LA-ICP-MS)

Laser-ablation inductively coupled plasma mass spectrometry (LA-ICP-MS) was used for trace element analyses of in-situ sphalerite, chalcopyrite, pyrrhotite, stannite, galena, and arsenopyrite ore assemblage from the Baal Gammon and Isabel deposits. Laser analyses were performed using an Analyte G2 Excimer Laser Ablation system coupled to a Thermo iCap-TQ ICP-MS instrument at the Advanced Analytical Centre, James Cook University. Laser ablation of the sulfides was carried out with an energy density of 2 J/cm^2 at a rate of 5 Hz on a spot size of 40 µm. NIST610 was analyzed and used as a reference standard, whereas MASS-1 and GSE-1 standards were used as external standards to monitor matrix effects. A mixture of helium and argon was used as the carrier gas for transporting the ablated analyte into the ICP-MS analysis chamber. A total of 39 isotopes were analyzed during spot analyses, and the major element concentrations (e.g., Cu for chalcopyrite and Zn for sphalerite) measured through electron microprobe. Kumar et al. (2023) was used as an internal standard during data reduction to yield quantitative element concentrations. The isotopes ^{113}In and ^{115}In were measured and the isobaric interference between ^{115}In and ^{115}Sn were monitored, and a correction factor was applied. The LA-ICP-MS trace element data was reduced using Iolite software (Paton et al. 2011; Fisher et al. 2017), and the laser peaks were inspected for spikes, which may indicate mineral inclusions. Summaries of the trace element results are provided in Tables 1 and 2.

Secondary ion mass spectrometry (SIMS)

The secondary ion mass spectrometry (SIMS) analysis of the in-situ chalcopyrite-pyrrhotite mineral pair for sulfur isotope ratios (^{32}S, ^{33}S, and ^{34}S) was performed on a CAMECA IMS1280 ion microprobe at the Centre for Microscopy Characterisation and Analysis at the University of Western Australia. Representative chalcopyrite and pyrrhotite ore samples from the Baal Gammon and Isabel deposits were mounted within 5 mm of the central portion of an epoxy mount that was cut at 1 cm from the edge to accommodate S isotope reference materials. The mount was thoroughly cleaned using distilled water and ethanol, then dried and coated with a 10-nm-thick gold layer.

During S isotope analysis, the sample surface was sputtered over a 10 × 10 µm area with a 10 kV, Gaussian Cs^+ beam at ~ 2 nA intensity and a total impact energy of 20 keV. Secondary ions were sputtered in the double focusing mass spectrometer within a 110 µm entrance slit and focused in the center of a 3000 µm field aperture (× 100 magnification). Energy filtering was performed using a 40 eV band pass, and a 5 eV gap was set toward the high-energy boundary. All S isotopes were collected simultaneously in Faraday cup detectors fitted with 10^{10} Ω (L'2, ^{32}S) and 10^{11} Ω (L1, ^{33}S and H1, ^{34}S) resistors, operating at a mass resolution of ~ 2500 amu. The $^{32}S^1H$ and ^{33}S peaks were not completely resolved under these conditions; thus, the magnetic field was offset slightly to the low-mass boundary to avoid interference from $^{32}S^1H$ on ^{33}S peaks. The magnetic field was regulated using a NMR control. Each analysis included a pre-sputtering measurement over a 15 × 15 µm area for 30

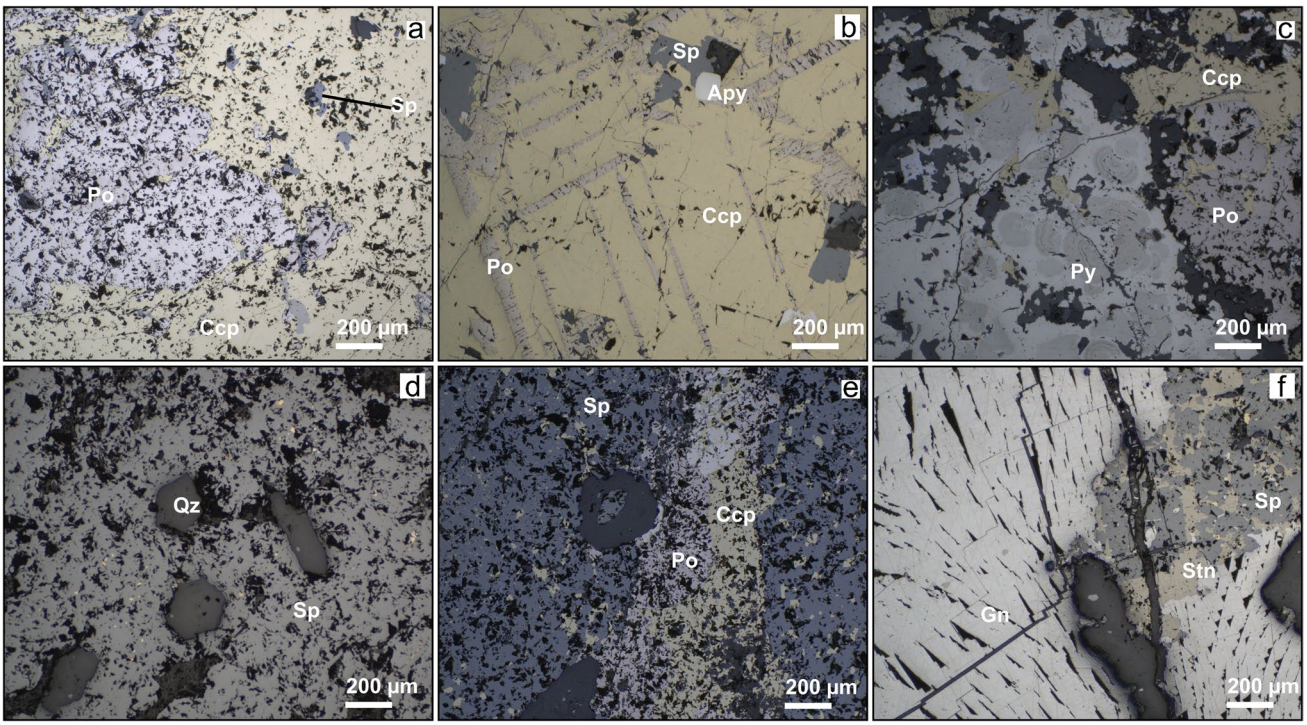

Fig. 5 Photomicrographs of ore samples from the Baal Gammon (**a**–**c**) and Isabel (**d**–**f**) deposits under reflected light. **a** Chalcopyrite (Ccp) and pyrrhotite (Po) with sphalerite (Sp) inclusions in massive sulfides at the contact of quartz-feldspar porphyry and UNA Porphyry. **b** Exsolution lamellae of pyrrhotite in chalcopyrite in sulfide veins located in the UNA Porphyry. **c** Framboidal pyrite (Py) in massive sulfides from the meta-sedimentary rocks. **d** Sphalerite (Sp) and quartz (Qz) in a hydrothermal breccia. **e** Sphalerite with thin veins of chalcopyrite and pyrrhotite. **f** Galena (Gn) vein with sphalerite and stannite (stn)

Table 1 A summary of trace element concentrations (ppm) for sulfide minerals from the Baal Gammon deposit

Mineral	Statistics	^{49}Ti	^{51}V	^{59}Co	^{66}Zn	^{69}Ga	^{73}Ge	^{77}Se	^{107}Ag	^{111}Cd	^{115}In	^{118}Sn	^{121}Sb
Chalcopyrite ($n = 30$)	Max	167	0.7	3.3	4331	3.9	5.6	60	821	24	1727	2354	5.9
	Min	141	0.2	2.0	727	2.2	3.2	45	345	6	1071	466	0.9
	Mean	153	0.4	2.6	2161	3.1	4.5	51	609	14	1194	1410	2.1
	SD	7	0.1	0.3	1211	0.4	0.6	3	172	6	122	350	1.1
Pyrrhotite ($n = 30$)	Max	174	0.8	135	51,818	10.1	8.4	35	225	40	4120	3359	13
	Min	129	0.5	105	1.6	0.3	5.7	25	0.8	0.01	0.01	0.3	0.4
	Mean	145	0.6	118	5394	3.4	6.8	30	46	18	815	493	3.9
	SD	8	0.1	10	11,124	2.5	0.7	2.4	57	14	927	956	3.1
Sphalerite ($n = 46$)	Max	248	1.3	91		22	1.7	42	321	3308	6795	13,013	36
	Min	76	0.2	35		1.7	0.1	17	10	1763	1658	1.5	0.2
	Mean	111	0.3	56		3.4	1.1	27	58	2717	2702	470	6.1
	SD	27	0.2	16		3.0	0.3	4.4	67	297	1135	1937	8.8
Arsenopyrite ($n = 15$)	Max	84	0.4	8607	-	-	4.4	139	26	0.28	1.0	1.5	1168
	Min	69	0.2	45	-	-	3.2	29	0.01	0.07	0.8	0.2	538
	Mean	73	0.3	1757	-	-	3.7	94	6	0.15	0.9	0.5	986
	SD	3.9	0.1	2312	-	-	0.4	33	9.3	0.11	0.1	0.6	181

- below the limit of detection, and blank fields represent major element

Table 2 A summary of trace element concentrations (ppm) for sulfide minerals from the Isabel deposit

Mineral	Statistics	^{49}Ti	^{51}V	^{59}Co	^{66}Zn	^{69}Ga	^{73}Ge	^{77}Se	^{107}Ag	^{111}Cd	^{115}In	^{118}Sn	^{121}Sb
Chalcopyrite ($n = 30$)	Max	170	3.0	0.9	43,093	54	8.8	21	2574	343	892	7841	23
	Min	119	0.2	0.1	355	0.5	3.3	14	2046	1.5	573	484	1.2
	Mean	139	0.7	0.3	4207	4.3	5.0	17	2302	26	725	1042	6.6
	SD	13	0.7	0.2	8109	10	1.0	1.8	145	63	80	1331	5.7
Pyrrhotite ($n = 30$)	Max	272	11	23	13,644	40	10	17	286	64	2182	12,151	632
	Min	126	0.4	18	10.11	0.3	5.2	2.6	8.3	0.04	0.1	0.9	1.1
	Mean	154	1.5	20	1138	8.4	7.0	6.8	79	6.3	290	1253	30
	SD	27	2.1	1.5	2503	11	1.0	3.5	86	12	470	2698	114
Sphalerite ($n = 61$)	Max	117	21	25		82	2.0	12	209	3195	1845	40,563	41
	Min	90	0.2	12		1.6	0.5	0.04	10	2143	569	1.5	0.1
	Mean	104	0.8	18		18	1.0	4.2	45	2695	1296	1747	7.4
	SD	6.6	3.0	3.9		15	0.3	3.7	42	299	456	6110	7.5
Galena ($n = 29$)	Max	38	0.2	-	305	-	-	7.7	4920	17	16	522	1447
	Min	13	0.02	-	0.4	-	-	1.1	389	5.2	0.7	130	416
	Mean	23	0.1	-	28	-	-	3.9	895	9.5	2.0	259	805
	SD	11	0.04	-	67	-	-	2.1	850	3.4	2.9	120	382
Stannite ($n = 31$)	Max	174	9.0	13	44,353	41	12	11	6070	544	4620	758,954	400
	Min	61	0.1	7.9	29,491	14	2.0	1.8	1618	191	2427	285,149	3.3
	Mean	85	0.7	10	39,325	22	5.0	3.3	2322	330	3184	333,479	61
	SD	24	1.9	1.8	3997	6.9	2.6	1.6	825	82	624	81,775	91

- below the limit of detection, and blank fields represent major element

s, and automated centering of the secondary ions in the field aperture, contrast aperture and entrance slit. Each analysis then consisted of 20 four-second cycles. The analytical session was monitored for drift using two bracketing standards after analysis of every five samples. Instrumental mass fractionation (IMF) was corrected using a matrix matched reference material (Nifty for chalcopyrite and Alexo for pyrrhotite, and reference values can be found in LaFlamme et al. (2016)). The used IMF correction procedures are detailed in LaFlamme et al. (2016) and Kita et al. (2009).

Geochemical modeling

Geochemical modeling of metal complexes and sulfide precipitation was conducted with The Geochemist's Workbench (GWB) Community Edition 13 (Bethke et al. 2022) software to investigate the: (1) stability of metal chlorides over a range of temperature and pH conditions and (2) sulfide ore formation as a function of sulfur fugacity (fS_2) and pH. The thermodynamic parameters (ΔG_f and K_{eq}) for modeling were taken from the default thermodynamic database contained in the GWB software. The metal chloride species that were modeled included Cu, Zn, Fe, and In complexes, with concentrations (10^{-6} M) similar to those observed in active hydrothermal systems (e.g., Seward et al. 2014; Simmons et al. 2016). The fS_2-pH phase diagrams for the sulfide ores were modeled for Cu, Zn, Fe, Co, and S between 0 and 300 °C. The modeling was focused on metal chloride complexes due to low-sulfidation character of these deposits, and the method was modified from Kumar et al. (2023) including temperature constraints.

Results

Petrographic observations

The mineral paragenesis (Fig. 4) and sulfide ore petrography (Fig. 5) shows that there are two types of chalcopyrite-pyrrhotite mineral pairs at Baal Gammon with only one type at Isabel. At Baal Gammon, the chalcopyrite-pyrrhotite mineral pairs include massive chalcopyrite in equilibrium with pyrrhotite (Fig. 5a), and chalcopyrite with pyrrhotite exsolution lamellae (Fig. 5b). Massive chalcopyrite in equilibrium with pyrrhotite was observed along the contact between the UNA Porphyry and the quartz-feldspar porphyry, and the meta-sedimentary rocks. Sulfide ore along the contact between the meta-sedimentary rocks and the UNA Porphyry contains minor amounts of pyrite, which consists of a framboidal core, likely of sedimentary origin, surrounded by an euhedral rim overgrowth (Fig. 5c). The

chalcopyrite grains with pyrrhotite exsolution lamellae are located in massive sulfide veins that crosscut the UNA Porphyry (Figs. 2d and 5b). Both types of chalcopyrite-pyrrhotite mineral pairs contain subhedral inclusions of sphalerite and cassiterite, with trace levels of arsenopyrite. Late arsenopyrite veins crosscut the earlier chalcopyrite veins and massive sulfide mineralization. In the Isabel deposit, chalcopyrite and pyrrhotite mineral pairs occur in thin veins that crosscut sphalerite mineralization (Fig. 5e).

Trace element composition of sulfides

Chalcopyrite, pyrrhotite, and sphalerite

The concentrations of trace element in chalcopyrite from both deposits are similar (Tables 1 and 2), except for Se, Cd, and In, which are distinctly higher at Baal Gammon. Minor variability was observed in the Ti, V, Co, Ga, Ge, Se, and Sb content of chalcopyrite grains from Baal Gammon. The average concentrations are 153 ppm for Ti, 0.4

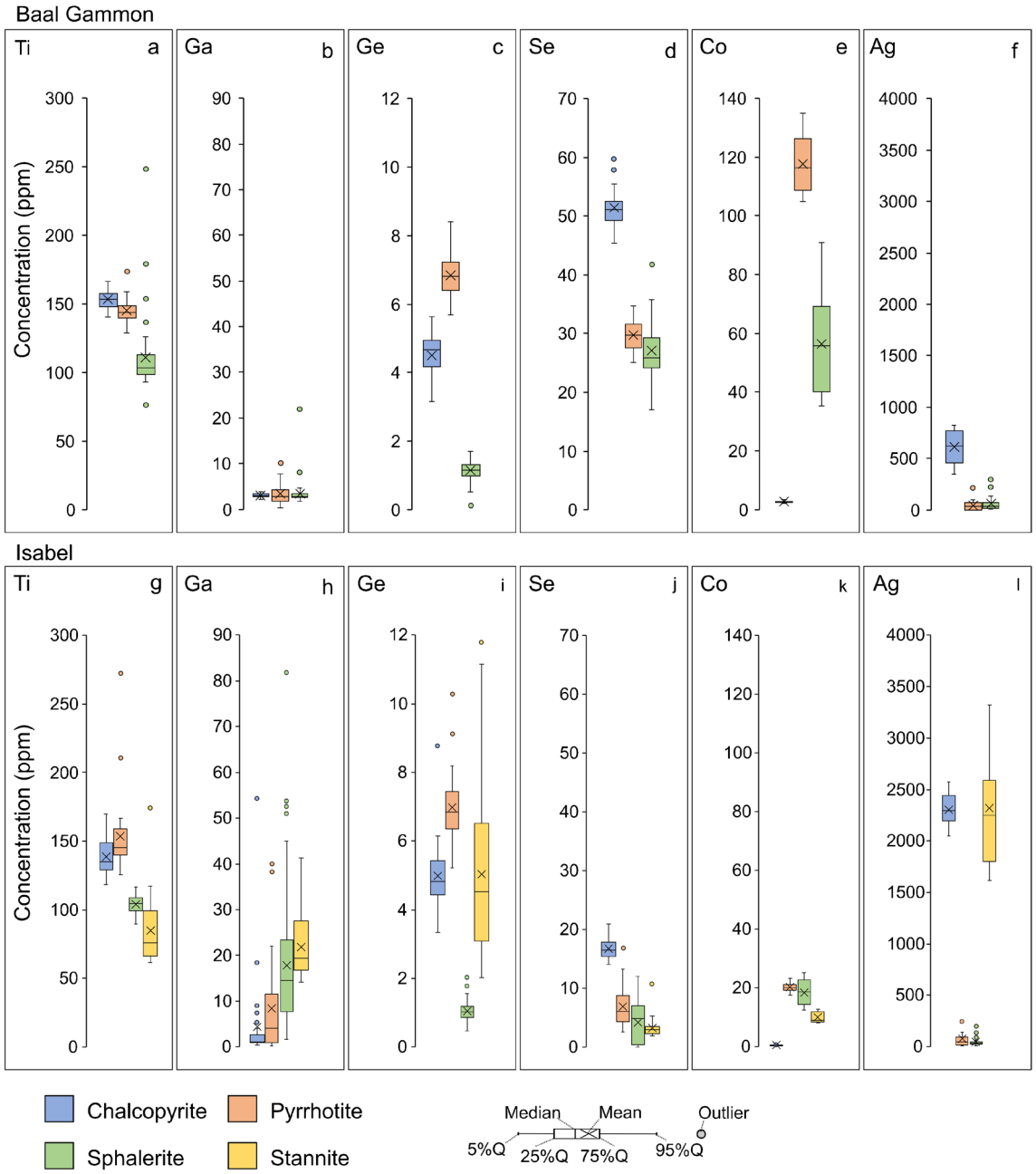

Fig. 6 Box and whiskers plot of trace elements (Ti, Ga, Ge, Se, Co, and Ag) concentrations (ppm) of chalcopyrite, pyrrhotite, sphalerite, and stannite from the Baal Gammon (**a**–**f**) and Isabel (**g**–**l**) deposits

ppm for V, 2.6 ppm for Co, 3.1 ppm for Ga, 4.5 ppm for Ge, 51 ppm for Se, and 2.1 ppm for Sb (Table 1, Fig. 6a–f). Silver, In, and Sn show large variations (Table 1; Fig. 6), with average concentrations of 609 ppm for Ag, 1194 ppm for In, and 1410 ppm for Sn. The average trace element content of Isabel chalcopyrite is 139 ppm for Ti, 0.7 ppm for V, 0.3 ppm for Co, 4.3 ppm for Ga, 5 ppm for Ge, 17 ppm for Se, 2302 ppm for Ag, 26 ppm for Cd, 725 ppm for In, 1042 ppm for Sn, and 6.6 ppm for Sb (Table 2, Fig. 6g–l).

The average content of trace elements for pyrrhotite is generally lower when compared to chalcopyrite except for Co (Table 2; Fig. 6). The Ti, V, Co, Ge, and Se contents in pyrrhotite from Baal Gammon show little variability, whereas the Ag, In, and Sn concentrations are highly variable. The average concentrations of these elements in pyrrhotite are 145 ppm Ti, 0.6 ppm V, 118 ppm Co, 6.8 ppm Ge, 30 ppm Se, 46 ppm Ag, 18 ppm Cd, 815 ppm In, and 493 ppm Sn (Table 1, Fig. 6a–f). The average concentration of trace elements in pyrrhotite from the Isabel deposit is 154 ppm Ti, 1.5 ppm V, 20 ppm Co, 7 ppm Ge, 6.8 ppm Se, 79 ppm Ag, 6.3 ppm Cd, 290 ppm In, 1253 ppm Sn, and 30 ppm Sb (Table 2).

The sphalerite grains from both deposits have similar trace element concentrations and show significant enrichment in Cd, In, and Sn. The Baal Gammon sphalerite inclusions in the massive sulfide ores contain, on average, 2702 ppm In, 2717 ppm Cd, and 470 ppm Sn, whereas sphalerite grains from the Isabel deposit contain, on average, 2695 ppm Cd, 1296 ppm In, and 1747 ppm Sn. The average trace element content of Baal Gammon sphalerite is 111 ppm Ti, 0.3 ppm V, 56 ppm Co, 3.4 ppm Ga, 1.1 ppm Ge, 27 ppm Se, 58 ppm Ag, and 6.1 ppm Sb (Table 1, Fig. 6a–f), whereas the average trace element content for sphalerite from Isabel is 104 ppm Ti, 0.8 ppm V, 18 ppm Co, 18 ppm Ga, 1.0 ppm Ge, 4.2 ppm Se, 45 ppm Ag, and 7.4 ppm Sb (Table 2).

Other sulfides

Other sulfide grains that were analyzed for trace element content included arsenopyrite from Baal Gammon and galena and stannite from Isabel. The arsenopyrite (Table 1) is enriched in Co (45–8607 ppm, avg. 1757 ppm) and Sb (538–1168 ppm, avg. 986 ppm). The galena from Isabel (Table 2) is enriched in Ag (389–4920 ppm, avg. 895 ppm) and Sb (416–1447 ppm, avg. 805 ppm). Stannite from Isabel (Table 2) is enriched in Ag (1618–6070 ppm, avg. 2322 ppm) and In (2427–4620 ppm, avg. 3184 ppm).

Sulfur isotope composition of chalcopyrite and pyrrhotite

A summary of the sulfur isotope data for the Baal Gammon and Isabel deposits is presented in Fig. 7. Sulfur isotope

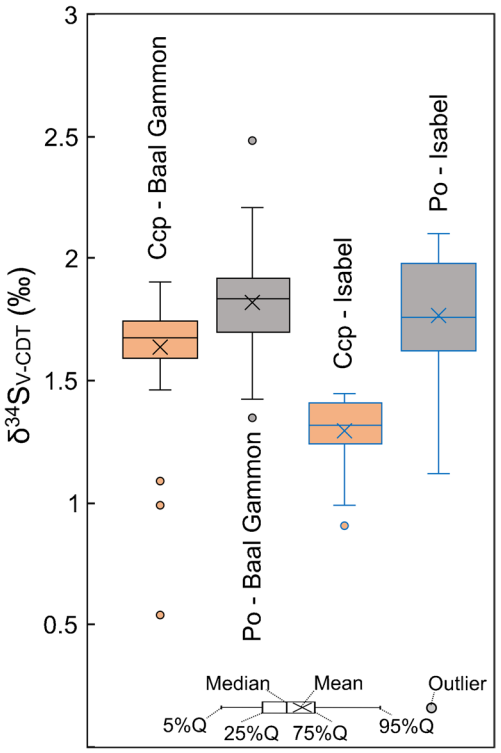

Fig. 7 Sulfur isotope box and whiskers plot of chalcopyrite (Ccp) and pyrrhotite (Po) from the Baal Gammon and Isabel deposits

analyses for chalcopyrite from the Baal Gammon and Isabel deposits returned $\delta^{34}S$ values ranging from + 0.54 to + 1.91‰ ($n = 52$) and + 0.91 to + 1.45‰ ($n = 18$), respectively. The 95% uncertainty confidence level for a single spot analysis of chalcopyrite is 0.04‰, and 0.07‰ for pyrrhotite.

At the Baal Gammon deposit, the $\delta^{34}S$ signature of chalcopyrite from massive sulfide located along the contact between the UNA Porphyry and the quartz-feldspar porphyry yields values of 0.99–1.91‰ with an average of 1.71 ± 0.54‰ ($n = 16$). The chalcopyrite grains from sulfide veins cross cutting the UNA Porphyry, and from the contact zone between meta-sedimentary rocks and the UNA Porphyry yield similar isotope values, which range from 1.46 to 1.74‰ (one outlier at 0.5‰) with an average of 1.63 ± 0.16‰ ($n = 21$). Chalcopyrite grains from the Isabel deposit yield $\delta^{34}S$ values between 0.91 and 1.45‰ with an average of 1.30 ± 0.29‰ ($n = 18$).

The values of $\delta^{34}S$ in pyrrhotite grains from the Baal Gammon and Isabel deposits are similar and range from 1.35 to 2.48‰ ($n = 51$) for the Baal Gammon deposit, and 1.12 to 2.11‰ ($n = 17$) for the Isabel deposit. The values of $\delta^{34}S$ in pyrrhotite grains from massive sulfide along the contact between the UNA Porphyry and quartz-feldspar porphyry range from 1.68 to 2.21‰ with an average of 1.94 ± 0.26‰ ($n = 16$). The $\delta^{34}S$ values of pyrrhotite from sulfide veins in the deeper section of the UNA Porphyry vary from

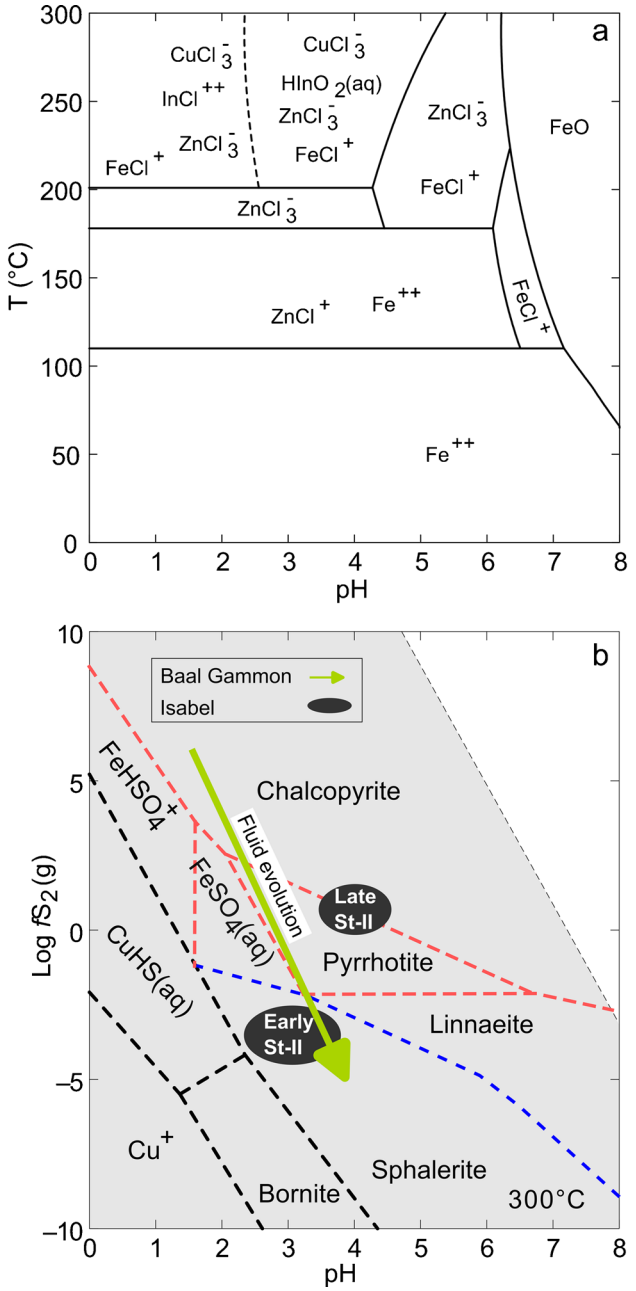

Fig. 8 **a** Stability field of metal-chloride complexes at 0–300 °C between pH 0 and 8. The metal-Cl decay over temperature and pH was constructed in The Geochemist's Workbench (Bethke et al. 2022) at conditions: $[Cu^{2+}] = 10^{-5}$, $[Zn^{2+}] = 10^{-5}$, $[Fe^{2+}] = 10^{-5}$, $[In^{3+}] = 10^{-5}$, $[Cl^{-}] = 0.1$, pressure = 1 bar and H_2O at unity. **b** Log fS_2 vs. pH plot for the key sulfide minerals at the Baal Gammon and Isabel deposits. The fS_2 plot was constructed using The Geochemist's Workbench (Bethke et al. 2022) at conditions: $[Cu^{2+}] = 10^{-5}$, $[Zn^{2+}] = 10^{-5}$, $[Fe^{2+}] = 10^{-5}$, $[Co^{2+}] = 10^{-5}$, $[SO_4^{2-}] = 10^{-5}$, temperature = 300 °C, pressure = 1 bar and H_2O at unity. The black, red, and blue boundary lines define Cu, Fe, and Zn species, respectively

1.42 to 2.48‰ with an average of 1.79 ± 0.43‰ ($n = 20$). The $\delta^{34}S$ values in pyrrhotite from the contact zone between meta-sedimentary rocks and the UNA Porphyry range from 1.12 to 2.11‰ with an average of 1.77 ± 0.50‰ ($n = 17$).

pH, Eh, and fS_2 modeling

The results obtained from geochemical modeling are presented in Fig. 8 as metal chloride and ore mineral stability field diagrams. The modeling indicates that chlorine complexes of Cu, Zn, and Fe at 300 °C are stable at pH ranges between 0 and 6, which is in agreement with pH and metal concentration values measured in geothermal waters of New Zealand (Simmons et al. 2016). In addition, In speciation is strongly linked to the pH of the hydrothermal fluids, in which In chlorine complexes were found to be stable only under acidic conditions at pH < 2 (Fig. 8a; Kumar et al. 2023). Modeling of the ore minerals indicates that chalcopyrite formed at a higher fS_2 compared to pyrrhotite and sphalerite, which confirms the paragenetic relationships observed at Baal Gammon and Isabel (Fig. 8b).

Discussion

The incorporation of trace elements in sulfide ores and temperature of ore formation

Trace element in hydrothermal sulfide grains can reside as solid and fluid inclusions, lattice-bound, and or absorbed constituents in the mineral structure (Fan et al. 2022; Lehrmann et al. 2022). It can be difficult to differentiate the residence state of trace elements in minerals, but inferences can be made from trace element variability. High variability on spot analyses indicates the presence of mineral or fluid inclusions. In contrast, a good element-element correlation indicates lattice-bound substitution. At Baal Gammon, chalcopyrite is the major Cu mineral and contains significant quantities (> 1000 ppm) of Zn (avg. 2161 ppm and SD at 1211 ppm), Ag (avg. 609 ppm and SD at 172 ppm), In (avg. 1194 ppm and SD at 122 ppm), and Sn (avg. 1410 ppm and SD at 350 ppm). There is little compositional variability in these elements (Table 1), which indicates lattice-bound substitution in most analyzed sulfide minerals.

The substitution of Zn, Sn, Ag, and In in chalcopyrite depends upon a number of factors including the ionic radii of the elements and the temperature and physicochemical conditions of the mineralizing fluids. Chalcopyrite from some VMS deposits in Eastern Australia shows substitution of Zn, In, and Sn for Fe, and Ag for Cu (Huston et al. 1995). The ionic radii of Zn, In, and Sn are within the acceptable range for substitution of Fe^{3+} and Fe^{2+} in chalcopyrite (George et al. 2018). Moderately strong correlations of Ag, In, and Sn with Fe (Fig. 9a) are likely indicative of coupled substitutions (Fig. 9a). Apart from the valency of Fe (3^+ and 2^+), the valence state of Cu in chalcopyrite is also debatable and both $Cu^{2+}Fe^{2+}(S^{2-})_2$ and $Cu^{+}Fe^{3+}(S^{2-})_2$ can occur (Todd et al. 2003; Pearce et al. 2006), but Li et al. (2013) suggested that

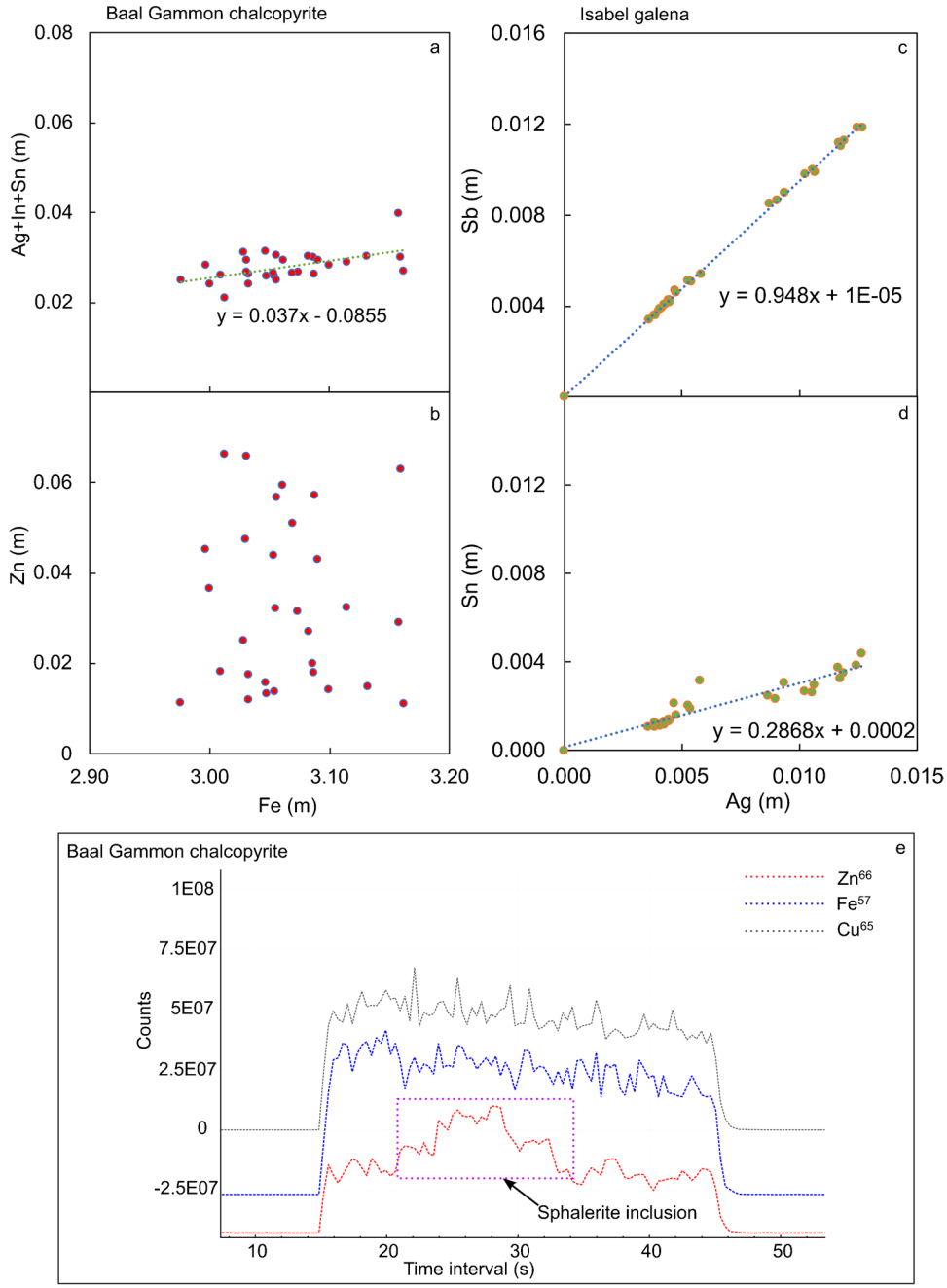

Fig. 9 Element correlation plots for chalcopyrite from Baal Gammon (**a**, **b**) and galena from Isabel (**c**, **d**). **a** Ag+In+Sn vs. Fe; **b** Zn vs. Fe; **c** Sb vs. Ag; **d** Sn vs. Ag; and **e** an example of time-resolved depth profile showing Zn spike related to sphalerite inclusions in Baal Gammon chalcopyrite. Element concentration on correlation plots is in molality (m)

intermediate valence states are likely favorable. Chalcopyrite with an intermediate valence state (Klekovkina et al. 2014) is likely present at Baal Gammon, where trivalent In and tetravalent Sn substitutes divalent and trivalent Fe, whereas the monovalent Ag most likely substitutes monovalent and divalent Cu.

The elements, Zn, Ag, In and Sn, when present in high concentrations (> 10,000 ppm), occur mainly as micron-sized inclusions (10–200 µm) of stannite and sphalerite that can be detected by scanning electron microscope (Kumar et al. 2022). The lack of correlation on Zn vs. Fe plot (Fig. 9b, e), highlights the occurrence of Zn as sphalerite inclusions. The average Cd concentration of Baal Gammon sphalerite is 2717 ppm with a low variability (Table 1) indicating a lattice-bound residence. The temperature and redox conditions of Cd substitution is poorly understood, and Cd^{2+} when substituted for Zn^{2+} leads to crystallographic deformation of the sphalerite unit cell as Zn^{2+} has an ionic radius of 0.74 Å, whereas Cd^{2+} has 0.95 Å (Wright 2009; Babedi et al. 2019, 2021). According to Goldschmidt's rules, trace element substitution in crystal lattice is preferred for elements with < 15% difference in ionic radius (e.g., George

et al. 2018; Zhang et al. 2021), but the difference in ionic radius of Cd^{2+} and Zn^{2+} is > 15%, and this substitution pathway may cause deformation in the mineral structure (Babedi et al. 2019). No sphalerite deformation was observed in Baal Gammon massive sulfides, and crystal habits are mostly euhedral or partially terminated (Fig. 5a–c), which indicates a lack of crystallographic deformation, and the substitution of Fe^{2+} by Cd^{2+} was favored. Other trace elements that are anomalous in the sulfides are Co and Cd, and they have higher affinity for pyrrhotite and sphalerite, respectively, than for chalcopyrite. The ionic radius of Co (Co^{2+} at 0.72 Å) is within range for substitution with Fe (Fe^{2+} at 0.74 Å; Dehaine et al. 2021), but only small amounts of Co (avg. 2.6 ppm) were detected in chalcopyrite (Fig. 6). In contrast, pyrrhotite contains an average of 118 ppm Co, where it likely substitutes for Fe.

At the Isabel deposit, sphalerite grains have high Cd, In, and Sn concentrations (Table 2). The Cd and In show low variability (Table 2) and are likely lattice bound. Tin is both lattice-bound and occurs as solid inclusions of cassiterite and or stannite since it has a higher variability (Table 2). The incorporation of Cd, In, and Sn in the sphalerite structure has been previously reported (Ingles and Mavrogenes 2021; Xu et al. 2021; Zhang et al. 2022), with In^{3+} substitution suggested to occur coupled with Cu^{+} (e.g., Cook et al. 2012; Bauer et al. 2019). The galena is cogenetic with sphalerite and formed in the early-stage II sulfide ores and contains high concentrations of Ag and Sb. The Sb vs. Ag plot shows a linear correlation (Fig. 9), indicating the presence of coupled substitution. Coupled substitution of Ag^{+} and Sb^{3+} for $2Pb^{2+}$ has been confirmed by multiple studies on trace elements in galena (e.g., Sharp and Buseck 1993; George et al. 2015; Liu et al. 2021). A linear trend is also seen on the Sn vs. Ag plot indicating the possibility of Sn incorporation in galena via coupled substitution. Tin substitution in galena has not been reported in the literature but our data indicates a possibility and Sn^{4+} has a similar ionic radius to Sb^{3+} (George et al. 2016), which further supports this substitution despite the difference in charge between the two ions. Possible mechanisms for this include coupled substitution of Sn^{4+} and $2Ag^{+}$ for $3Pb^{2+}$, or Sn^{2+} and $2Ag^{+}$ for $2Pb^{2+}$, or direct substitution of Pb^{2+} by Sn^{2+}.

Evolution of ore fluids at the Baal Gammon and Isabel deposits

The trace element composition of the major sulfides together with thermodynamic modeling of the Baal Gammon and Isabel deposits can be used to deduce the evolution of the mineralizing fluids. In both deposits, the ore textures indicate a hydrothermal origin for the mineralization and most metals discussed so far are transported as metal chloride complexes in natural hydrothermal systems at very low concentrations (Hedenquist et al. 1993). Our physicochemical modeling suggests that Cu, Zn, and Fe chlorine complexes are favored at pH ≤ 6 between 200 and 300 °C (Fig. 8a), which is consistent with observations from active hydrothermal systems (e.g., Simmons et al. 2016; Grant et al. 2020), whereas In chloride complexes are only stable at pH < 3. The incorporation of large amounts of In in chalcopyrite indicates that, at the time of chalcopyrite formation, the pH of the fluid was low (pH < 3) according to the physicochemical modeling (Fig. 8). Thus, chalcopyrite crystallization condition can be constrained to ~ 300 °C, at pH < 3 and high sulfur fugacity (Fig. 8). At the Baal Gammon deposit, textural evidence suggests that pyrrhotite and sphalerite are cogenetic with chalcopyrite, but their crystallization may have occurred in sequence as the fluid chemistry evolved (Fig. 8b). The sequence of sulfide crystallization likely occurred in this order, from first to last, chalcopyrite followed by pyrrhotite than sphalerite as inclusions, according to ore petrology (Fig. 5a–c) and geochemical modeling (Fig. 8b). The geochemical modeling indicates that during sulfide ore formation, the mineralizing fluid evolved toward a moderate pH and low sulfur fugacity (Fig. 8b). Based on element substitutions and the possibility of existence of multiple valence state of Cu and Fe in chalcopyrite ($Cu^{2+}Fe^{2+}(S^{2-})_2$ vs. $Cu^{+}Fe^{3+}(S^{2-})_2$), the redox conditions of the mineralizing fluids likely fluctuated along the redox boundary of Fe^{2+}/Fe^{3+} and Cu^{+}/Cu^{2+}.

At the Isabel deposit, the mineral paragenesis and cross-cutting relationships indicate that sphalerite and galena formed during early-stage II mineralization and were cross-cut by late, thin chalcopyrite and pyrrhotite veins (Figs. 4b and 5e). This suggests that stage II mineralization occurred by two distinct pulses of sulfidic fluid. The first pulse of the fluids was dominated by Zn and Pb that formed the large sphalerite and galena veins and occurred at low sulfur fugacity and moderate pH (Fig. 8b). The second pulse of fluids formed the late-stage II mineralization consisting of thin chalcopyrite and pyrrhotite veins (Figs. 4b and 5e) and records increasing sulfur fugacity and decreasing pH trends (Fig. 8b).

Sulfur and metal sources at the Baal Gammon and Isabel deposits

The texture of the sulfide mineralization (Figs. 2 and 5) together with sulfur isotopes (Figs. 7 and 10) of chalcopyrite and pyrrhotite can be used to make inferences about the source of sulfur during mineralization. At Baal Gammon, the variation in sulfur isotopes in chalcopyrite (+ 1.0 to + 1.9‰) and pyrrhotite (+ 1.4 to + 2.5‰) is small. Chalcopyrite, pyrrhotite, and pyrite from VMS and IOCG deposits show a wide variation in sulfur isotopes (5 to 20‰), which has been attributed to mixing of magmatic, connate, and

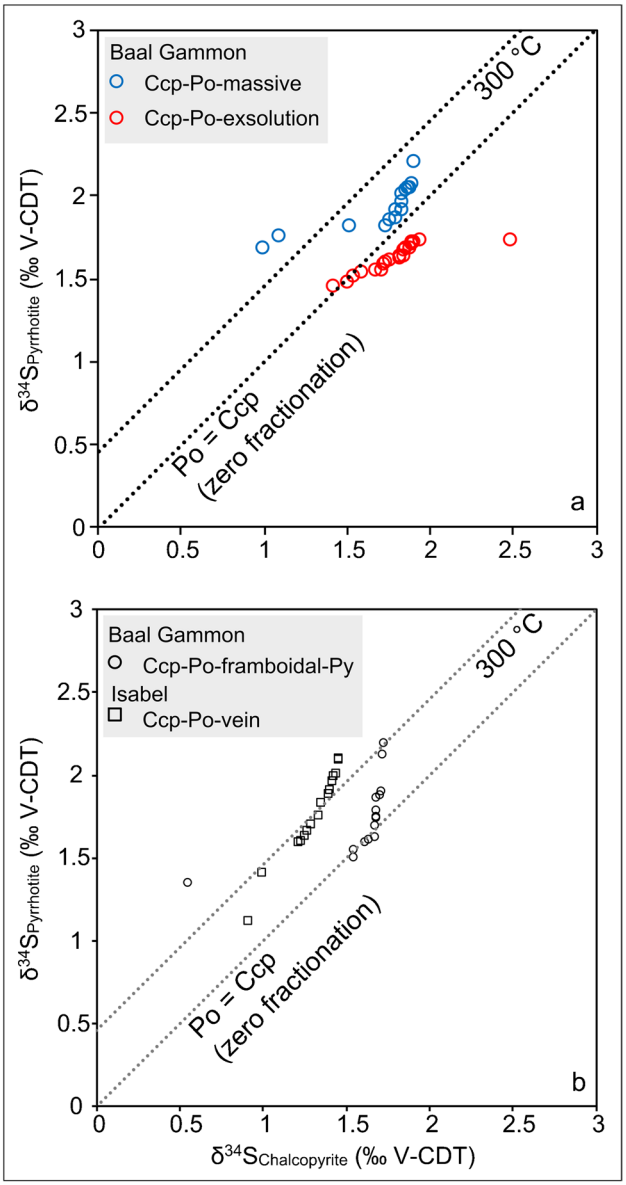

Fig. 10 δ-δ plots for chalcopyrite and pyrrhotite mineral pairs. **a** The Baal Gammon samples show disequilibrium fractionation of sulfur isotopes in massive chalcopyrite and pyrrhotite (Ccp-Po-massive) and chalcopyrite with pyrrhotite exsolution (Ccp-Po-exsolution). **b** The Baal Gammon sample containing framboidal pyrite (Ccp-Po-framboidal-Py) shows modified equilibrium fractionation, whereas the Isabel samples of chalcopyrite and pyrrhotite veins (Ccp-Po-vein) plot on the kinetic fractionation line of 300 °C from Kajiwara and Krouse (1971)

meteoric fluids (Brueckner et al. 2015; Li et al. 2021). Constrained sulfur isotope signatures were also observed in the cross-cutting chalcopyrite (+ 1 to + 1.5‰) and pyrrhotite (+ 1.1 to + 2.1‰) veins of the Isabel deposit. The Isabel deposit is dominated by sphalerite polymetallic veins and is distally related to the fluid source. The narrow sulfur isotope ranges of chalcopyrite and pyrrhotite from the Baal Gammon and Isabel deposits indicate a magmatic origin of the mineralizing fluids with minimal interaction with connate and meteoric waters. The magmatic source of the sulfur-bearing fluid is further supported by the sulfide mineralization being spatially and temporarily associated to the magmatic activity of the Slaughter Yard Creek Volcanics in the HMF (Kumar et al. 2022).

If the fractionation process was in equilibrium and kinetically driven, then the $\delta^{34}S$ of sulfide mineral pairs can be used to predict the temperature of formation (Kajiwara and Krouse 1971). An attempt was made (Fig. 10a), but it did not yield expected temperatures for the Baal Gammon deposit. For the Isabel deposit, the temperature predicted by the fractionation of $\delta^{34}S$ between chalcopyrite and pyrrhotite is ~ 300 ± 40 °C (Fig. 10b). The temperature of formation for the Baal Gammon deposit (290 ± 12 °C) from stannite-sphalerite thermometer obtained in Kumar et al. (2023) is very similar to the Isabel deposit. This confirms that sulfur isotope fractionation in the Baal Gammon massive sulfides occurred in disequilibrium since they do not plot on the kinetic fractionation line (Fig. 10). This disequilibrium is not surprising, especially in massive sulfide veins from the deeper parts of the UNA Porphyry (Fig. 5b), as chalcopyrite and pyrrhotite did not precipitate simultaneously, but pyrrhotite exsolved along the grain boundaries of chalcopyrite (Fig. 5). Isotopic disequilibrium caused by paragenetic mineral phase differences is widely recognized (Rye 2005) and could explain the sulfur isotope fractionation observed in massive sulfides at the Baal Gammon deposit.

The sulfur isotope pattern from the sedimentary section of the Baal Gammon massive sulfides shows a unique fractionation pattern between chalcopyrite and pyrrhotite (Fig. 10b), which is not compatible with kinetic or mass-dependent fractionation of stable isotopes. Sulfur isotopes can be fractionated by microbial activity to varying degrees, from 2 to 42‰, where the degree of fractionation depends upon the culture of microbes present (Detmers et al. 2001). The presence of framboidal pyrite (Fig. 5c) in the massive sulfides occurring in the meta-sedimentary rocks of the Baal Gammon deposit indicates the presence of microbial activity in the meta-sedimentary rocks. In sedimentary environments, microbe-derived framboidal pyrite has been used to approximate paleo-redox conditions (Chen et al. 2022). In our case, the framboidal pyrite is early, syn-sedimentary, and is overgrown by euhedral pyrite (Fig. 5c), indicating that they may not provide an accurate prediction of redox conditions associated with ore formation, but constitutes a local source of sulfur during the formation of massive sulfide ores at the contact between the UNA Porphyry and meta-sedimentary rocks. Thus, the sulfur isotope fractionation from massive sulfides at the meta-sedimentary rocks contact can be explained by interaction of fluids with sulfur derived from framboidal pyrite.

The low variation in the sulfur isotope data indicates that the bulk of the sulfur was derived from magmatic sources with only a negligible fraction derived from pre-existing syn-sedimentary framboidal pyrite. Magmatic activity that was cogenetic with sulfide mineralization occurred at ca. 288 Ma at Baal Gammon and ca. 292 Ma at Isabel, and regionally, this pulse peaked at ca. 285 Ma (Kumar et al. 2022). In the eastern part of the HMF, this magmatic pulse formed the Koolmoon Volcanic Group (Fig. 1) that consists of the Glen Gordon, Walsh Bluff, and Slaughter Yard Creek Volcanics near the Baal Gammon and Isabel deposits (Figs. 2 and 3). The trace element data from Cheng et al. (2018) indicate considerable amounts of Cu (~ 10 ppm), Zn (~ 10 ppm), W (~ 10 ppm), and Pb (~ 10 ppm) in the Slaughter Yard Creek Volcanics (Fig. 11b). This volcanic group plots above the dividing boundary of the magnetite series granite on the Fe_2O_3/FeO vs. Rb/Sr plot (Fig. 11a; Blevin et al. 1996; Baker et al. 2005). Therefore, these units were derived from a subvolcanic source with a strongly oxidized signature indicating a high potential for Cu-Mo and Mo mineralization (Blevin et al. 1996; Baker et al. 2005). Oxidized volcanic and felsic rocks associated with Cu mineralization indicate a likely magmatic origin for mineralizing fluids (Hattori and Keith 2001; Richards 2015). The presence of the Baal Gammon and Isabel deposits near oxidized magmatic and metal enriched rocks indicates a genetic association of Cu mineralization to the ca. 290 Ma Slaughter Yard Creek Volcanics unit (Kumar et al. 2022), whereas Sn is linked to the reduced 365–317 Ma O'Briens Creek Supersuite in the region (Fig. 11; Champion 1991; Cheng et al. 2018; Kumar et al. 2022).

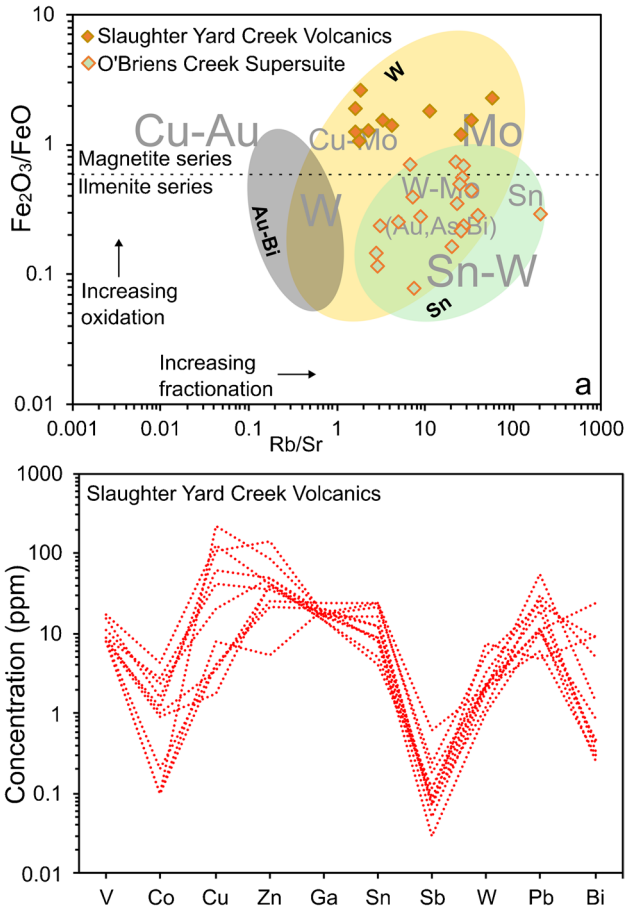

Fig. 11 **a** Oxidation and fractionation states of Slaughter Yard Creek Volcanics and O'Briens Creek Supersuite with geochemistry data from Cheng et al. (2018). The plot was adopted from Voudouris et al. (2022) and compiled from Baker et al. (2005), Blevin (2004), and Blevin et al. (1996). **b** Trace element concentration line plot of Slaughter Yard Creek Volcanics with data from Cheng et al. (2018)

Possible genetic model of Cu mineralization in the Herberton Mineral Field

Tin-Cu deposits occur in various tectonic settings, for example, the deposits in Cornwall, England, formed during an extensional phase in a collisional orogen, the San Rafael deposit in Peru formed in a subduction-related back-arc setting, the deposits in the Erzgebirge, Germany, formed in a post-collisional extensional zone, and deposits in Yunnan, China, formed in a back-arc, extensional setting (Sillitoe and Lehmann 2022). This suggests that Sn-Cu deposits can form in a variety of tectonic settings with a common presence of coeval magmatism. The latter provides the heat and fluid source and plays an important role in mobilizing metals and transporting metals to form Sn-Cu deposits with multiple heating/hydrothermal episodes recorded in most locations (Romer and Kroner 2016). Due to the complex nature of mineralizing processes resulting from multiple magmatic fluid pulses, most Sn-Cu deposits consist of complex mineral parageneses with likely several generations of mineralization, where Sn, Cu, Zn, and other metals are deposited in multiple stages. This understanding of Sn-Cu deposits allows us to systematically propose a Cu deposition model for the HMF.

The stages of ore paragenesis indicate decoupled Sn and Cu mineralization at the Baal Gammon and Isabel deposits. The Sn episode in the HMF is the earliest record of mineralization in the Kennedy Igneous Association and occurs in fractionated granites of the O'Briens Creek Supersuite (Figs. 1b, 11a and 12a). This episode lasted from 340 to 310 Ma, where the granites were emplaced in a compressional tectonic regime (Cheng et al. 2018; Kumar et al. 2022). Deposition of Sn is facilitated by reduced magmas (e.g., O'Briens Creek Supersuite, Fig. 11a) where Sn species were transported in acidic and reduced hydrothermal fluids (Heinrich 1990). Copper mineralization, in contrast, is promoted by oxidized magmas (Murakami and Ishihara 2013; Sillitoe and Lehmann 2022), which further supports the decoupled deposition

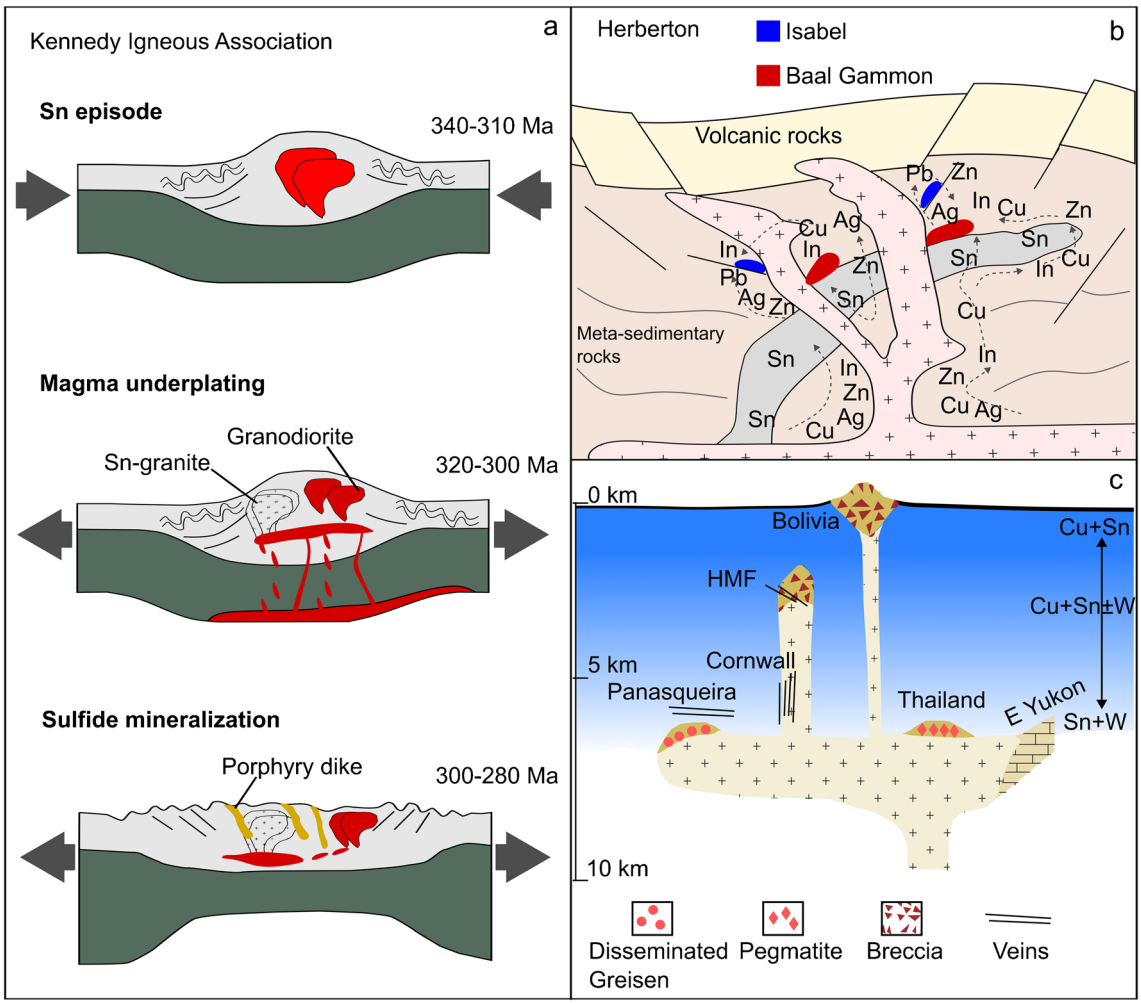

Fig. 12 **a** Tectonic synthesis of the HMF modified from Kumar et al. (2022). **b** Simplified genetic model of Cu mineralization in the HMF, showing intrusion of porphyry that caused sulfide mineralization. The metal pathway is indicated with arrows for the hydrothermal system that was likely active. **c** Schematic illustration of different mineralization styles in fractionated granites adopted from Baker et al. (2005), depicts metal (Cu, Sn and W) mineralization linked to depth

of Sn and Cu in the HMF. For these metal pairs to occur together, the reduced magma pool requires fertilization by mafic melts. Zircon geochronology by Kumar et al. (2022) showed that emplacement of granodiorite and other mafic-endmember granitic suites (Alamaden Supersuite; Fig. 1) occurred between 320 and 300 Ma in the HMF. The emplacement of these granodiorite units in the HMF (Fig. 12a), in combination with Nd and Hf isotope anomalies observed in the regional granites, suggests a magmatic recharge between 320 and 300 Ma (Champion and Bultitude 2013; Cheng et al. 2018). This magmatic recharge was likely caused by magma underplating that fertilized the reduced magma pool (Fig. 12a). Magma underplated fertilization of a reduced magma pool has been observed in other Sn-Cu deposits, such as the San Rafael deposit in Peru (Harlaux et al. 2021b), deposits in the Andean Sn belt (Sillitoe and Lehmann 2022), and the Tongshanling deposit in Nanling Range, China (Wu et al. 2021). Following this, an episode of tectonic extension and crustal thinning between 300 and 280 Ma supplied the heat that generated the Slaughter Yard Creek Volcanics in the HMF (Fig. 12a; Kumar et al. 2022). The Slaughter Yard Creek Volcanics were generated from a fertile protolith that formed oxidizing magma and deposited sulfide and critical metals in the HMF.

The intrusion of the Slaughter Yard Creek Volcanics allowed access to the necessary ingredients, such as magmatic sulfur, chlorine, and heat to initiate the hydrothermal cycling of Cu, Zn, In, Ag, Fe, and Pb chlorine ligand complexes that were deposited as magmatic-hydrothermal polymetallic deposits in the HMF (Fig. 12b). The deposition of chalcopyrite in acidic condition caused alteration of

the wall rock that is evidenced by silicification at the Baal Gammon and Isabel deposits (Kumar et al. 2022, 2023). Similar alteration and mineralization patterns were observed in the Cornwall ore field (Müller et al. 2006) and the Bolivian Sn-Cu field (Fig. 12c; Torró et al. 2019b, Torró et al. 2019a; Torres et al. 2019). In these styles of Sn deposits that are mostly related to fractionated granites, Cu mineralization is strongly linked to depths above ~ 5 km (Fig. 12c; Baker et al. 2005).

Conclusion

The Baal Gammon and Isabel deposits show that Sn and Cu mineralization in the HMF were derived from different sources. Field evidence and petrology of ore samples indicate that Sn is early, whereas Cu is a late phase of sulfide mineralization. The sulfide mineralization is closely associated with the emplacement of the Slaughter Yard Creek Volcanics, whereas Sn is present in the UNA Porphyry in the Baal Gammon deposit. Constrained low sulfur isotope values indicate that the mineralizing fluids were magmatically derived with little interaction with connate water. The sulfur isotopes and textures of chalcopyrite and pyrrhotite from the UNA Porphyry and the Slaughter Yard Creek Volcanics indicate possible interaction of sulfidic fluid with Sn mineralization. The temperature of the sulfide mineralization was estimated from the sulfur isotopes of the Isabel deposit at 300 °C. The chalcopyrite shows high concentrations of trace element compared to pyrrhotite in the Baal Gammon deposit. The intrusive porphyries of the Slaughter Yard Creek Volcanics played a role in the evolution of the hydrothermal-magmatic event that formed Cu mineralization in the HMF.

Acknowledgements We thank the Economic Geology Research Centre (EGRU) at James Cook University (Townsville), Red River Resources Ltd., and Dr Yi Hu at Advanced Analytical Centre (AAC) at James Cook University for aiding us in analyzing sulfide ores via LA-ICP-MS.

Author contribution Fieldwork was conducted by AAK and IS; analyses were conducted by AAK, LM, and MA; manuscript conceptualization, illustration, and was jointly written by AAK, IS, and LM; text edited and modified by PHGMD.

Funding Open Access funding enabled and organized by CAUL and its Member Institutions The Geological Survey of Queensland supported this study as part of the New Economy Minerals Initiative. AAK was supported by a Commonwealth Research scholarship at James Cook University.

Data availability Supplementary material related to this article can be found at https://doi.org/10.25903/cmt0-b449, an integrated data management platform hosted at Research Data JCU.

Declarations

Conflict of interest The authors declare no competing interests.

References

Audétat A, Günther D, Heinrich CA (2000) Causes for large-scale metal zonation around mineralized plutons: fluid inclusion LA-ICP-MS evidence from the Mole Granite, Australia. Econ Geol 95:1563–1581. https://doi.org/10.2113/gsecongeo.95.8.1563

Babedi L, Tadie M, Neethling P, von der Heyden BP (2021) A fundamental assessment of the impacts of cation (Cd, Co, Fe) substitution on the molecular chemistry and surface reactivity of sphalerite. Miner Eng 160:106695. https://doi.org/10.1016/j.mineng.2020.106695

Babedi L, von der Heyden BP, Neethling PH, Tadie M (2019) The effect of Cd- substitution on the Raman vibrational characteristics of sphalerite. Vib Spectrosc 105:102968. https://doi.org/10.1016/j.vibspec.2019.102968

Baker T, Pollard PJ, Mustard R et al (2005) A comparison of granite-related tin, tungsten, and gold-bismuth deposits: implications for exploration. SEG Discovery:5–17. https://doi.org/10.5382/SEGnews.2005-61.fea

Barnes S-J, Lightfoot PC (2005) Formation of magmatic nickel sulfide deposits and processes affecting their copper and platinum group element contents. In: One Hundredth Anniversary Volume. Society of Economic Geologists

Bauer ME, Seifert T, Burisch M et al (2019) Indium-bearing sulfides from the Hämmerlein skarn deposit, Erzgebirge, Germany: evidence for late-stage diffusion of indium into sphalerite. Miner Depos 54:175–192. https://doi.org/10.1007/s00126-017-0773-1

Bethke CM, Farrell B, Yeakel S (2022) The Geochemist's Workbench, Version 12.0: GWB essentials guide. LLC Champaign, Illinois, US

Blake DH (1972) Regional and economic geology of the Herberton/Mount Garnet area-Herberton Tinfield, North Queensland: B.M.R. Australia Bulletin 124:1–11

Blevin PL (2004) Redox and compositional parameters for interpreting the granitoid metallogeny of eastern Australia: implications for gold-rich ore systems. Resour Geol 54:241–252. https://doi.org/10.1111/J.1751-3928.2004.TB00205.X

Blevin PL, Chappell BW, Allen CM (1996) Intrusive metallogenic provinces in eastern Australia based on granite source and composition. Earth Environ Sci Trans R Soc Edinb 87:281–290. https://doi.org/10.1017/S0263593300006684

Brown AC (1997) World-class sediment-hosted stratiform copper deposits: characteristics, genetic concepts and metallotects. Aust J Earth Sci 44:317–328. https://doi.org/10.1080/08120099708728315

Brown AC (2014) Low-temperature sediment-hosted copper deposits. In: Treatise on geochemistry. Elsevier, pp 251–271

Brueckner SM, Piercey SJ, Layne GD et al (2015) Variations of sulphur isotope signatures in sulphides from the metamorphosed Ming Cu(−Au) volcanogenic massive sulphide deposit, Newfoundland Appalachians, Canada. Miner Depos 50:619–640. https://doi.org/10.1007/s00126-014-0567-7

Cawood PA (2005) Terra Australis Orogen: Rodinia breakup and development of the Pacific and Iapetus margins of Gondwana during the Neoproterozoic and Paleozoic. Earth Sci Rev 69:249–279. https://doi.org/10.1016/j.earscirev.2004.09.001

Champion DC (1991) The felsic granites of far north Queensland. (PhD thesis). The Australian National University, Canberra, Australia

Champion DC, Bultitude RJ (2013) The geochemical and Sr-Nd isotopic characteristics of Paleozoic fractionated S-types granites of north Queensland: implications for S-type granite petrogenesis. Lithos 162–163:37–56. https://doi.org/10.1016/j.lithos.2012.11.022

Champion DC, Chappell BW (1992) Petrogenesis of felsic I-type granites: an example from northern Queensland. Spec Pap Geol Soc Am 272:115–126. https://doi.org/10.1130/SPE272-p115

Chen Z, Fang Y, Wignall PB et al (2022) Microbial blooms triggered pyrite framboid enrichment and oxygen depletion in carbonate platforms immediately after the Latest Permian Extinction. Geophys Res Lett 49. https://doi.org/10.1029/2021GL096998

Cheng Y, Spandler C, Chang Z, Clarke G (2018) Volcanic–plutonic connections and metal fertility of highly evolved magma systems: a case study from the Herberton Sn–W–Mo Mineral Field, Queensland, Australia. Earth Planet Sci Lett 486:84–93. https://doi.org/10.1016/j.epsl.2018.01.012

Chiaradia M, Caricchi L (2022) Supergiant porphyry copper deposits are failed large eruptions. Commun Earth Environ 3:107. https://doi.org/10.1038/s43247-022-00440-7

Cook NJ, Ciobanu CL, Brugger J et al (2012) Determination of the oxidation state of Cu in substituted Cu-In-Fe-bearing sphalerite via μ-XANES spectroscopy. Am Min 97:476–479. https://doi.org/10.2138/am.2012.4042

Cross AJ, Purdy DJ, Champion DC et al (2018) Insights into the evolution of the Thomson Orogen from geochronology, geochemistry, and zircon isotopic studies of magmatic rocks. Aust J Earth Sci 65:987–1008. https://doi.org/10.1080/08120099.2018.1515791

Dehaine Q, Tijsseling LT, Glass HJ et al (2021) Geometallurgy of cobalt ores: a review. Miner Eng 160:106656. https://doi.org/10.1016/j.mineng.2020.106656

Detmers J, Brüchert V, Habicht KS, Kuever J (2001) Diversity of sulfur isotope fractionations by sulfate-reducing Prokaryotes. Appl Environ Microbiol 67:888–894. https://doi.org/10.1128/AEM.67.2.888-894.2001

Dill HG, Garrido MM, Melcher F et al (2013) Sulfidic and non-sulfidic indium mineralization of the epithermal Au–Cu–Zn–Pb–Ag deposit San Roque (Provincia Rio Negro, SE Argentina) — with special reference to the "indium window" in zinc sulfide. Ore Geol Rev 51:103–128. https://doi.org/10.1016/j.oregeorev.2012.12.005

Dirks HN, Sanislav IV, Sharib AS (2021) Continuous convergence along the paleo-Pacific margin of Australia during the Early Paleozoic: insights from the Running River Metamorphics, NE Queensland. Lithos 398–399:106343. https://doi.org/10.1016/j.lithos.2021.106343

Eckstrand OR, Hulbert LJ (2007) Magmatic nickel-copper-platinum group element deposits. In: Goodfellow WD (ed) Mineral deposits of Canada: a synthesis of major deposit types, district metallogeny, the evolution of geological provinces, and exploration methods: Geological Association of Canada, Mineral Deposits Division, Special Publication No. 5, p 205–222

Edgar A, Sanislav IV, Dirks PH (2022a) Tectonic setting and mineralisation potential of the Cowley Ophiolite Complex, north Queensland. Aust J Earth Sci 1–17:1132–1148. https://doi.org/10.1080/08120099.2022.2086173

Edgar A, Sanislav IV, Dirks PH, Spandler C (2022b) Metamorphic diamond from the northeastern margin of Gondwana: paradigm shifting implications for one of Earth's largest orogens. Sci Adv 8:2811. https://doi.org/10.1126/sciadv.abo2811

Edgar A, Sanislav I, Dirks P (2023) The origin of mafic–ultramafic rocks and felsic plutons along the Clarke River suture zone: implications for porphyry exploration in the northern Tasmanides. Aust J Earth Sci 1–16. https://doi.org/10.1080/08120099.2023.2234964

Elshkaki A, Graedel TE, Ciacci L, Reck BK (2016) Copper demand, supply, and associated energy use to 2050. Glob Environ Change 39:305–315. https://doi.org/10.1016/j.gloenvcha.2016.06.006

Etschmann BE, Liu W, Testemale D et al (2010) An in situ XAS study of copper(I) transport as hydrosulfide complexes in hydrothermal solutions (25–592 °C, 180–600 bar): speciation and solubility in vapor and liquid phases. Geochim Cosmochim Acta 74:4723–4739. https://doi.org/10.1016/j.gca.2010.05.013

Eugster HP (1985) Granites and hydrothermal ore deposits: a geochemical framework. Mineral Mag 49:7–23. https://doi.org/10.1180/minmag.1985.049.350.02

Fan L, Wang G, Holzheid A et al (2022) Systematic variations in trace element composition of pyrites from the 26°S hydrothermal field, Mid-Atlantic Ridge. Ore Geol Rev 148. https://doi.org/10.1016/j.oregeorev.2022.105006

Farquhar J, Wu N, Canfield DE, Oduro H (2010) Connections between sulfur cycle evolution, sulfur isotopes, sediments, and base metal sulfide deposits. Econ Geol 105:509–533. https://doi.org/10.2113/gsecongeo.105.3.509

Fisher CM, Paton C, Pearson DG et al (2017) Data reduction of Laser Ablation Split-Stream (LASS) analyses using newly developed features within Iolite: with applications to Lu-Hf + U-Pb in detrital zircon and Sm-Nd +U-Pb in igneous monazite. Geochem Geophys Geosystems 18:4604–4622. https://doi.org/10.1002/2017GC007187

Fitzherbert JA, McKinnon AR, Blevin PL et al (2021) The Hera orebody: a complex distal (Au–Zn–Pb–Ag–Cu) skarn in the Cobar Basin of central New South Wales, Australia. Resource Geology 71:296–319. https://doi.org/10.1111/rge.12262

Flöttmann T, Haines P, Jago J et al (1998) Formation and reactivation of the Cambrian Kanmantoo Trough, SE Australia: implications for early Palaeozoic tectonics at eastern Gondwana's plate margin. J Geol Soc London 155:525–539. https://doi.org/10.1144/gsjgs.155.3.0525

Flöttmann T, James P, Rogers J, Johnson T (1994) Early Palaeozoic foreland thrusting and basin reactivation at the Palaeo-Pacific margin of the southeastern Australian Precambrian Craton: a reappraisal of the structural evolution of the Southern Adelaide Fold-Thrust Belt. Tectonophysics 234:95–116. https://doi.org/10.1016/0040-1951(94)90206-2

Foden J, Elburg M, Turner S et al (2020) Cambro-Ordovician magmatism in the Delamerian orogeny: implications for tectonic development of the southern Gondwanan margin. Gondwana Res 81:490–521. https://doi.org/10.1016/j.gr.2019.12.006

George L, Cook NJ, Cristiana C, Wade BP (2015) Trace and minor elements in galena: a reconnaissance LA-ICP-MS study. Am Min 100:548–569. https://doi.org/10.2138/am-2015-4862

George LL, Cook NJ, Ciobanu CL (2016) Partitioning of trace elements in co-crystallized sphalerite–galena–chalcopyrite hydrothermal ores. Ore Geol Rev 77:97–116. https://doi.org/10.1016/j.oregeorev.2016.02.009

George LL, Cook NJ, Crowe BBP, Ciobanu CLL (2018) Trace elements in hydrothermal chalcopyrite. Mineral Mag 82:59–88. https://doi.org/10.1180/minmag.2017.081.021

Glen RA (2005) The Tasmanides of eastern Australia. Geol Soc Spec Publ 246:23–96. https://doi.org/10.1144/GSL.SP.2005.246.01.02

Glen RA, Korsch RJ, Hegarty R et al (2013) Geodynamic significance of the boundary between the Thomson Orogen and the Lachlan Orogen, northwestern New South Wales and implications for Tasmanide tectonics. Aust J Earth Sci 60:371–412. https://doi.org/10.1080/08120099.2013.782899

Gómez ALR, Ulrich T, Rubinstein NA (2021) The magmatic–hydrothermal evolution of the San Pedro porphyry Cu-(Mo) deposit: implications for the metallogenesis of the Permian magmatism in the western margin of Gondwana. Res Geol 71:93–104. https://doi.org/10.1111/rge.12251

Grant HLJ, Hannington MD, Hardardóttir V et al (2020) Trace metal distributions in sulfide scales of the seawater-dominated Reykjanes geothermal system: constraints on sub-seafloor hydrothermal mineralizing processes and metal fluxes. Ore Geol Rev 116:103145. https://doi.org/10.1016/j.oregeorev.2019.103145

Gray DR, Foster DA (2004) Tectonic evolution of the Lachlan Orogen, southeast Australia: historical review, data synthesis and modern perspectives. Aust J Earth Sci 51:773–817. https://doi.org/10.1111/j.1400-0952.2004.01092.x

Han C, Xiao W, Zhao G et al (2006) Major types, characteristics and geodynamic mechanism of Upper Paleozoic copper deposits in northern Xinjiang, northwestern China. Ore Geol Rev 28:308–328. https://doi.org/10.1016/j.oregeorev.2005.04.002

Harlaux M, Kouzmanov K, Gialli S et al (2021a) Fluid mixing as primary trigger for cassiterite deposition: evidence from in situ $\delta^{18}O$-$\delta^{11}B$ analysis of tourmaline from the world-class San. Earth Planet Sci Lett 563:116889. https://doi.org/10.1016/j.epsl.2021.116889

Harlaux M, Kouzmanov K, Gialli S et al (2021b) The upper Oligocene San Rafael intrusive complex (Eastern Cordillera, southeast Peru), host of the largest-known high-grade tin deposit. Lithos 400–401:106409. https://doi.org/10.1016/j.lithos.2021.106409

Hattori KH, Keith JD (2001) Contribution of mafic melt to porphyry copper mineralization: evidence from Mount Pinatubo, Philippines, and Bingham Canyon, Utah, USA. Miner Depos 36:799–806. https://doi.org/10.1007/s001260100209

Hedenquist JW, Simmons SF, Giggenbach WF, Eldridge CS (1993) White Island, New Zealand, volcanic-hydrothermal system represents the geochemical environment of high-sulfidation Cu and Au ore deposition. Geology 21:731. https://doi.org/10.1130/0091-7613(1993)021<0731:WINZVH>2.3.CO;2

Heinrich CA (1990) The chemistry of hydrothermal tin(-tungsten) ore deposition. Econ Geol 85:457–481. https://doi.org/10.2113/gsecongeo.85.3.457

Henderson RA, Donchak PJT, Withnall IW (2013) Mossman Orogen. In: Jell PA (ed) Geology of Queensland. Geological Survey of Queensland, pp 225–304

Hough MA, Bierlein FP, Wilde AR (2007) A review of the metallogeny and tectonics of the Lachlan Orogen. Miner Depos 42:435–448. https://doi.org/10.1007/s00126-006-0073-7

Huston DL, Sie SH, Suter GF et al (1995) Trace elements in sulfide minerals from eastern Australian volcanic-hosted massive sulfide deposits; Part I, Proton microprobe analyses of pyrite, chalcopyrite, and sphalerite, and Part II, Selenium levels in pyrite; comparison with delta 34 S values and implications for the source of sulfur in volcanogenic hydrothermal systems. Econ Geol 90:1167–1196. https://doi.org/10.2113/gsecongeo.90.5.1167

Ingles CH, Mavrogenes JA (2021) Cationic substitutions in sphalerite from the Porgera mine, Papua New Guinea. Can Mineral 59:573–587. https://doi.org/10.3749/canmin.2000085

Ishihara S (1981) The granitoid series and mineralization. In: Seventy-fifth anniversary volume. Society of Economic Geologists, pp 458–484

Jessop K, Daczko NR, Piazolo S (2019) Tectonic cycles of the New England Orogen, eastern Australia: a review. Aust J Earth Sci 66:459–496. https://doi.org/10.1080/08120099.2018.1548378

Kajiwara Y, Krouse HR (1971) Sulfur isotope partitioning in metallic sulfide systems. Can J Earth Sci 8:1397–1408. https://doi.org/10.1139/e71-129

Kelly WC, Turneaure FS (1970) Mineralogy, paragenesis and geothermometry of the tin and tungsten deposits of the eastern Andes, Bolivia. Econ Geol 65:609–680. https://doi.org/10.2113/gsecongeo.65.6.609

Kirkham RV, Sinclair WD (1995) Porphyry copper, gold, molybdenum, tungsten, tin, silver. In: Sinclair WD, Thorpe RI (eds) Eckstrand OR. Geology of Canadian mineral deposit types. Geological Society of America, pp 421–446

Kita NT, Ushikubo T, Fu B, Valley JW (2009) High precision SIMS oxygen isotope analysis and the effect of sample topography. Chem Geol 264:43–57. https://doi.org/10.1016/j.chemgeo.2009.02.012

Klekovkina VV, Gainov RR, Vagizov FG et al (2014) Oxidation and magnetic states of chalcopyrite $CuFeS_2$: a first principles calculation. Opt Spectrosc 116:885–888. https://doi.org/10.1134/S0030400X14060149

Klootwijk C (2013) Middle–Late Paleozoic Australia–Asia convergence and tectonic extrusion of Australia. Gondwana Res 24:5–54. https://doi.org/10.1016/j.gr.2012.10.007

Kojima S, Trista-Aguilera D, Hayashi K (2009) Genetic aspects of the manto-type copper deposits based on geochemical studies of North Chilean deposits. Resour Geol 59:87–98. https://doi.org/10.1111/j.1751-3928.2008.00081.x

Kumar AA, Sanislav IV, Cathey HE, Dirks PHGM (2023) Geochemistry of indium in magmatic-hydrothermal tin and sulfide deposits of the Herberton Mineral Field. Miner Depos, Australia. https://doi.org/10.1007/s00126-023-01179-7

Kumar AA, Sanislav IV, Dirks PH (2022) The geological setting of the indium-rich Baal Gammon and Isabel Sn-Cu-Zn deposits in the Herberton Mineral Field, Queensland, Australia. Ore Geol Rev 149:105095. https://doi.org/10.1016/j.oregeorev.2022.105095

Labidi J, Cartigny P, Hamelin C et al (2014) Sulfur isotope budget (^{32}S, ^{33}S, ^{34}S and ^{36}S) in Pacific–Antarctic ridge basalts: a record of mantle source heterogeneity and hydrothermal sulfide assimilation. Geochim Cosmochim Acta 133:47–67. https://doi.org/10.1016/j.gca.2014.02.023

LaFlamme C, Martin L, Jeon H et al (2016) In situ multiple sulfur isotope analysis by SIMS of pyrite, chalcopyrite, pyrrhotite, and pentlandite to refine magmatic ore genetic models. Chem Geol 444:1–15. https://doi.org/10.1016/j.chemgeo.2016.09.032

Lehmann B (2021) Formation of tin ore deposits: a reassessment. Lithos 402–403:105756. https://doi.org/10.1016/j.lithos.2020.105756

Lehrmann B, Cooper MJ, Milton JA, Murton BJ (2022) Formation, remobilisation and alteration processes at inactive hydrothermal vents: insights from elemental analysis of Cu-(Fe-)S sulfides from TAG, Mid-Atlantic Ridge. Miner Depos 57(8):1431–1448. https://doi.org/10.1007/s00126-022-01106-2

Li J, Hu R, Xiao J et al (2020) Genesis of gold and antimony deposits in the Youjiang metallogenic province, SW China: evidence from in situ oxygen isotopic and trace element compositions of quartz. Ore Geol Rev 116:103257. https://doi.org/10.1016/j.oregeorev.2019.103257

Li R, Chen H, Wu N et al (2021) Multiple sulfur isotopes in post-Archean deposits as a potential tracer for fluid mixing processes: an example from an iron oxide–copper–gold (IOCG) deposit in southern Peru. Chem Geol 575:120230. https://doi.org/10.1016/j.chemgeo.2021.120230

Li Y, Kawashima N, Li J et al (2013) A review of the structure, and fundamental mechanisms and kinetics of the leaching of chalcopyrite. Adv Colloid Interface Sci 197–198:1–32. https://doi.org/10.1016/j.cis.2013.03.004

Liu W, McPhail DC (2005) Thermodynamic properties of copper chloride complexes and copper transport in magmatic-hydrothermal solutions. Chem Geol 221:21–39. https://doi.org/10.1016/j.chemgeo.2005.04.009

Liu Z, Mao X, Wang F et al (2021) Deciphering anomalous Ag enrichment recorded by galena in Dayingezhuang Au(-Ag) deposit, Jiaodong Peninsula, Eastern China. Trans Nonferrous Met Soc China 31:3831–3846. https://doi.org/10.1016/S1003-6326(21)65768-0

Meinert LD (1992) Skarns and skarn deposits. Geosci Can 19:145–162

Mosier DL, Berger VI, Singer DA (2009) Volcanogenic massive sulfide deposits of the world – database and grade and tonnage models. USGS Open File Report 2009–1034

Müller A, Seltmann R, Halls C et al (2006) The magmatic evolution of the Land's End pluton, Cornwall, and associated pre-enrichment of metals. Ore Geol Rev 28:329–367. https://doi.org/10.1016/j.oregeorev.2005.05.002

Murakami H, Ishihara S (2013) Trace elements of Indium-bearing sphalerite from tin-polymetallic deposits in Bolivia, China and Japan: a femto-second LA-ICPMS study. Ore Geol Rev 53:223–243. https://doi.org/10.1016/j.oregeorev.2013.01.010

Nguyen RT, Eggert RG, Severson MH, Anderson CG (2021) Global electrification of vehicles and intertwined material supply chains of cobalt, copper and nickel. Resour Conserv Recycl 167:105198. https://doi.org/10.1016/j.resconrec.2020.105198

Ohmoto H (1972) Systematics of sulfur and carbon isotopes in hydrothermal ore deposits. Economic Geology 67:551–578. https://doi.org/10.2113/gsecongeo.67.5.551

Paton C, Hellstrom J, Paul B et al (2011) Iolite: freeware for the visualisation and processing of mass spectrometric data. J Anal At Spectrom 26:2508. https://doi.org/10.1039/c1ja10172b

Pearce CI, Pattrick RAD, Vaughan DJ et al (2006) Copper oxidation state in chalcopyrite: mixed Cu d^9 and d^{10} characteristics. Geochim Cosmochim Acta 70:4635–4642. https://doi.org/10.1016/j.gca.2006.05.017

Pokrovski GS, Borisova AY, Bychkov AY (2013) Speciation and transport of metals and metalloids in geological vapors. Rev Mineral Geochem 76:165–218. https://doi.org/10.2138/rmg.2013.76.6

Purdy DJ, Cross AJ, Brown DD et al (2016) New constraints on the origin and evolution of the Thomson Orogen and links with central Australia from isotopic studies of detrital zircons. Gondwana Res 39:41–56. https://doi.org/10.1016/j.gr.2016.06.010

Rajabpour S, Abedini A, Alipour S et al (2017a) Geology and geochemistry of the sediment-hosted Cheshmeh-Konan redbed-type copper deposit, NW Iran. Ore Geol Rev 86:154–171. https://doi.org/10.1016/j.oregeorev.2017.02.013

Rajabpour S, Behzadi M, Jiang S-Y et al (2017b) Sulfide chemistry and sulfur isotope characteristics of the Cenozoic volcanic-hosted Kuh-Pang copper deposit, Saveh county, northwestern central Iran. Ore Geol Rev 86:563–583. https://doi.org/10.1016/j.oregeorev.2017.03.001

Richards JP (2011) Magmatic to hydrothermal metal fluxes in convergent and collided margins. Ore Geol Rev 40:1–26. https://doi.org/10.1016/j.oregeorev.2011.05.006

Richards JP (2015) The oxidation state, and sulfur and Cu contents of arc magmas: implications for metallogeny. Lithos 233:27–45. https://doi.org/10.1016/j.lithos.2014.12.011

Richards JP (2016) Clues to hidden copper deposits. Nat Geosci 9:195–196. https://doi.org/10.1038/ngeo2656

Richards JP, Mumin AH (2013) Magmatic-hydrothermal processes within an evolving Earth: iron oxide-copper-gold and porphyry Cu ± Mo ± Au deposits. Geology 41:767–770. https://doi.org/10.1130/G34275.1

Romer RL, Kroner U (2016) Phanerozoic tin and tungsten mineralization—tectonic controls on the distribution of enriched protoliths and heat sources for crustal melting. Gondwana Res 31:60–95. https://doi.org/10.1016/j.gr.2015.11.002

Rosenbaum G (2018) The Tasmanides: Phanerozoic tectonic evolution of Eastern Australia. Annu Rev Earth Planet Sci 46:291–325. https://doi.org/10.1146/annurev-earth-082517-010146

Rye RO (2005) A review of the stable-isotope geochemistry of sulfate minerals in selected igneous environments and related hydrothermal systems. Chem Geol 215:5–36. https://doi.org/10.1016/j.chemgeo.2004.06.034

Schaarschmidt A, Haase KM, Klemd R et al (2021) Boiling effects on trace element and sulfur isotope compositions of sulfides in shallow-marine hydrothermal systems: evidence from Milos Island, Greece. Chem Geol 583:120457. https://doi.org/10.1016/j.chemgeo.2021.120457

Seal RR (2006) Sulfur isotope geochemistry of sulfide minerals. Rev Mineral Geochem 61:633–677. https://doi.org/10.2138/rmg.2006.61.12

Seward TM, Williams-Jones AE, Migdisov AA (2014) The chemistry of metal transport and deposition by ore-forming hydrothermal fluids, 2nd edn. Elsevier Ltd.

Shanks WCP, Slack JF, Till AB et al (2014) Sulfur and oxygen isotopic study of Paleozoic sediment-hosted Zn-Pb(-Ag-Au-Ba-F) deposits and associated hydrothermal alteration zones in the Nome Complex, Seward Peninsula, Alaska. In: Dumoulin JA, Till AB (eds) Reconstruction of a Late Proterozoic to Devonian continental margin sequence, Northern Alaska, its paleogeographic significance, and contained base-metal sulfide deposits. Geological Society of America, pp 235–256

Sharp TG, Buseck PR (1993) The distribution of Ag and Sb in galena: inclusions versus solid solution. Am Min 78:85–95

Sillitoe RH (2010) Porphyry copper systems. Econ Geol 105:3–41. https://doi.org/10.2113/gsecongeo.105.1.3

Sillitoe RH, Lehmann B (2022) Copper-rich tin deposits. Miner Depos 57:1–11. https://doi.org/10.1007/s00126-021-01078-9

Simmons SF, Brown KL, Tutolo BM (2016) Hydrothermal transport of Ag, Au, Cu, Pb, Te, Zn, and other metals and metalloids in New Zealand geothermal systems: spatial patterns, fluid-mineral equilibria, and implications for epithermal mineralization. Econ Geol 111:589–618. https://doi.org/10.2113/econgeo.111.3.589

Singer DA (2017) Future copper resources. Ore Geol Rev 86:271–279. https://doi.org/10.1016/j.oregeorev.2017.02.022

Skirrow RG (2022) Iron oxide copper-gold (IOCG) deposits – a review (part 1): settings, mineralogy, ore geochemistry and classification. Ore Geol Rev 140:104569. https://doi.org/10.1016/j.oregeorev.2021.104569

Spampinato GPT, Ailleres L, Betts PG, Armit RJ (2015a) Crustal architecture of the Thomson Orogen in Queensland inferred from potential field forward modelling. Aust J Earth Sci 62:581–603. https://doi.org/10.1080/08120099.2015.1063546

Spampinato GPT, Betts PG, Ailleres L, Armit RJ (2015b) Early tectonic evolution of the Thomson Orogen in Queensland inferred from constrained magnetic and gravity data. Tectonophysics 651–652:99–120. https://doi.org/10.1016/j.tecto.2015.03.016

Sun W, Liang H, Ling M et al (2013) The link between reduced porphyry copper deposits and oxidized magmas. Geochim Cosmochim Acta 103:263–275. https://doi.org/10.1016/j.gca.2012.10.054

Tashi M, Mousivand F, Ghasemi H et al (2021) Evolution of the Garmab-e-Paein native copper-rich volcanogenic massive sulfide deposit from northeast Iran: insights from sulfur isotope and chlorite chemistry. Ore Geol Rev 138:104345. https://doi.org/10.1016/j.oregeorev.2021.104345

Taylor R, Cuff C (1979) Geology of tin deposits. Elsevier, Amsterdam, pp 1–50

Todd EC, Sherman DM, Purton JA (2003) Surface oxidation of chalcopyrite ($CuFeS_2$) under ambient atmospheric and aqueous (pH 2-10) conditions: Cu, Fe L- and O K-edge X-ray spectroscopy. Geochim Cosmochim Acta 67:2137–2146. https://doi.org/10.1016/S0016-7037(02)01371-6

Tornos F, Peter JM, Allen R, Conde C (2015) Controls on the siting and style of volcanogenic massive sulphide deposits. Ore Geol Rev 68:142–163. https://doi.org/10.1016/j.oregeorev.2015.01.003

Torres B, Melgarejo JC, Torró L et al (2019) The Poopó polymetallic epithermal deposit, Bolivia: mineralogy, genetic constraints, and distribution of critical elements. Minerals 9:472. https://doi.org/10.3390/min9080472

Torró L, Cazorla M, Melgarejo JC et al (2019a) Indium mineralization in the volcanic dome-hosted Ánimas–Chocaya–Siete Suyos polymetallic deposit, Potosí, Bolivia. Minerals 9:604. https://doi.org/10.3390/min9100604

Torró L, Melgarejo J, Gemmrich L et al (2019b) Spatial and temporal controls on the distribution of indium in xenothermal vein-deposits: the Huari Huari District, Potosí, Bolivia. Minerals 9:304. https://doi.org/10.3390/min9050304

Tostevin R, Turchyn AV, Farquhar J et al (2014) Multiple sulfur isotope constraints on the modern sulfur cycle. Earth Planet Sci Lett 396:14–21. https://doi.org/10.1016/j.epsl.2014.03.057

VandenBerg AHM (1999) Timing of orogenic events in the Lachlan Orogen. Aust J Earth Sci 46:691–701. https://doi.org/10.1046/j.1440-0952.1999.00738.x

Voudouris P, Repstock A, Spry PG et al (2022) Physicochemical constraints on indium-, tin-, germanium-, gallium-, gold-, and tellurium-bearing mineralizations in the Pefka and St Philippos polymetallic vein- and breccia-type deposits, Greece. Ore Geol Rev 140:104348. https://doi.org/10.1016/j.oregeorev.2021.104348

Walker AT, Evans KA, Kirkland CL et al (2019) Tracking mineralisation with in situ multiple sulphur isotopes: a case study from the Fraser Zone, Western Australia. Precambrian Res 332:105379. https://doi.org/10.1016/j.precamres.2019.105379

Watari T, Nansai K, Nakajima K (2020) Review of critical metal dynamics to 2050 for 48 elements. Resour Conserv Recycl 155:104669. https://doi.org/10.1016/j.resconrec.2019.104669

White AJR, Allen CM, Beams SD et al (2001) Granite suites and supersuites of eastern Australia. Aust J Earth Sci 48:515–530. https://doi.org/10.1046/j.1440-0952.2001.00874.x

Withnall IW, Henderson RA (2012) Accretion on the long-lived continental margin of northeastern Australia. Episodes 35:166–176. https://doi.org/10.18814/epiiugs/2012/v35i1/016

Wright K (2009) The incorporation of cadmium, manganese and ferrous iron in sphalerite: insights from computer simulations. Can Mineral 47:615–623. https://doi.org/10.3749/canmin.47.3.615

Wu J, Kong H, Li H et al (2021) Multiple metal sources of coupled Cu-Sn deposits: insights from the Tongshanling polymetallic deposit in the Nanling Range, South China. Ore Geol Rev 139:104521. https://doi.org/10.1016/j.oregeorev.2021.104521

Xie J, Tang D, Qian L et al (2020) Geochemistry of sulfide minerals from skarn Cu (Au) deposits in the Fenghuangshan ore field, Tongling, eastern China: insights into ore-forming process. Ore Geol Rev 122:103537. https://doi.org/10.1016/j.oregeorev.2020.103537

Xu J, Cook NJ, Ciobanu CL et al (2021) Indium distribution in sphalerite from sulfide–oxide–silicate skarn assemblages: a case study of the Dulong Zn–Sn–In deposit, Southwest China. Miner Depos 56:307–324. https://doi.org/10.1007/s00126-020-00972-y

Zhang P, Peng B, Zhao J et al (2022) Genesis of the Bayan Qagan Dongshan Sn-Pb-Zn-Ag deposit, NE China, based on sphalerite chemistry and sulfur isotope. Ore Geol Rev 150:105124. https://doi.org/10.1016/j.oregeorev.2022.105124

Zhang X, Fang Z, Yang H et al (2021) Lattice evolution, ordering transformation and microwave dielectric properties of rock-salt $Li_{3+x}Mg_{2-2x}Nb_{1-x}Ti_{2x}O_6$ solid-solution system: a newly developed pseudo ternary phase diagram. Acta Mater 206:116636. https://doi.org/10.1016/j.actamat.2021.116636

Zhou Z, Wen H (2021) A magmatic-hydrothermal indium-bearing polymetallic vein mineralization belt in the western Jiangnan Orogen: evidence from zinc and cadmium isotopes of sphalerite. Ore Geol Rev 131:103843. https://doi.org/10.1016/j.oregeorev.2020.103843